A THESIS SUBMITTED TO
THE GRADUATE SCHOOL OF NATURAL AND APPLIED SCIENCES
OF ÇANKIRI KARATEKİN UNIVERSITY

PRODUCING FERRONICKEL VIA DIRECT REDUCTION OF GÖRDES LATERITE IN FLUIDIZED BED REACTOR

IN PARTIAL FULFILLMENT OF THE REQUIREMENTS
FOR
THE DEGREE OF MASTER OF SCIENCE
IN
CHEMICAL ENGINEERING

BY

BASHAR MOHAMMED MOHAMMED JABER ALSABAK

ÇANKIRI

2023

PRODUCING FERRONICKEL VIA DIRECT REDUCTION OF GÖRDES LATERITE IN FLUIDIZED BED REACTOR

By Bashar MOHAMMED MOHAMMED JABER ALSABAK

February 2023

We certify that we have read this thesis and that in our opinion it is fully adequate, in scope and in quality, as a thesis for the degree of Master of Science

Advisor **:** Assoc. Prof. Dr. Nesibe DİLMAÇ

Examining Committee Members:

Chairman **:** Assoc. Prof. Dr. Nesibe DİLMAÇ
Chemical Engineering
Çankırı Karatekin University

Member **:** Assoc. Prof. Dr. Zehra ÖZBAŞ
Chemical Engineering
Çankırı Karatekin University

Member **:** Assoc. Prof. Dr. Mehmet Selçuk MERT
Energy Systems Engineering
Yalova University

Approved for the Graduate School of Natural and Applied Sciences

Prof. Dr. Hamit ALYAR
Director of Graduate School

I hereby declare that all information in this document has been obtained and presented in accordance with academic rules and ethical conduct. I also declare that, as required by these rules and conduct, I have fully cited and referenced all material and results that are not original to this work.

Bashar MOHAMMED MOHAMMED JABER ALSABAK

ABSTRACT

PRODUCING FERRONICKEL VIA DIRECT REDUCTION OF GÖRDES LATERITE IN FLUIDIZED BED REACTOR

Bashar MOHAMMED MOHAMMED JABER ALSABAK

Master of Science in Chemical Engineering

Advisor: Assoc. Prof. Dr. Nesibe DİLMAÇ

February 2023

In this study, the laterite ore supplied from Manisa Gördes mine was crushed and calcined, afterward the calcined ore was reduced at a fluidized bed reactor by H_2 stream with a volumetric rate 6 times the minimum fluidization velocity and the reaction kinetics of the process was determined. The reduction tests were performed at 700, 750, 800 and 850 ºC reaction temperatures using 10%, 25% and 40% H_2 concentrations. The reduction degree of the ore was calculated with the help of the instantaneous concentration of gas streams leaving the reactor. The obtained "Time-Reduction Degree" graphs revealed that the process is more sensitive to H_2 concentration compared to the temperature, this finding supports the idea that the process proceeded mainly under diffusion control. Detailed kinetic analysis revealed that the reduction consisted of 3 stages; the first progressed under chemical reaction control according to the "Contracting Sphere, R3(α)" model (E_a=34.76 kJ/mol), and the second progressed under diffusion control according to the "One Dimensional Diffusion, D1(α)" model (E_a=10.18 kJ/mol). No model representing the third stage, which proceeds with an extremely low reaction rate, has been found. The sintering caused by the high reaction temperature and the hardly reducable nature of the trevorite mineral in the ore limited the highest reduction degree obtained in this study to 81%.

2023, 39 pages

Keywords: Direct reduction, Laterite, Ferronickel, Fluidized bed, Reaction kinetics

ÖZET

GÖRDES LATERİT CEVHERİNİN AKIŞKAN YATAK REAKTÖRDE DİREKT İNDİRGENMESİ İLE FERRONİKEL ELDE EDİLMESİ

Bashar MOHAMMED MOHAMMED JABER ALSABAK
Kimya Mühendisliği, Yüksek Lisans
Tez Danışmanı: Doç. Dr. Nesibe DİLMAÇ
Şubat 2023

Bu çalışmada, Manisa Gördes yataklarından temin edilen ve kırılarak kalsine edilen laterit cevheri akışkan yatak reaktörde, minimum akışkanlaşma hızının 6 katı debiye sahip H_2 akımı ile indirgenerek prosese ait reaksiyon kinetiği belirlenmiştir. Deneylerde 700, 750, 800 ve 850 ºC şeklinde 4 ayrı reaksiyon sıcaklığında ve %10, %25 ve %40 şeklinde 3 ayrı H_2 konsantrasyonunda çalışılmıştır. Cevherin indirgenme derecesi reaktörden çıkan gaz akımlarının anlık konsantrasyonu yardımıyla hesaplanmıştır. Elde edilen "Zaman-İndirgenme Derecesi" grafikleri, prosesin sıcaklığa nazaran H_2 konsatrasyonuna daha duyarlı olduğunu ortaya koymuş, bu bulgu prosesin ağırlıklı olarak difüzyon kontrolü altında ilerlediği fikrini desteklemiştir. Detaylı kinetik analiz, indirgenmenin 3 aşamadan oluştuğunu, ilk aşamanın "Büzülen Küre, R3(α)" modeline uygun olarak kimyasal reaksiyon kontrolü altında ilerlediğini (E_a=34,76 kJ/mol), ikinci aşamanın ise "Tek Boyutlu Difüzyon, D1(α)" modeline uygun olarak difüzyon kontrolü altında ilerlediğini (E_a=10,18 kJ/mol) ortaya koymuştur. Son derece düşük reaksiyon hızıyla ilerleyen üçüncü aşamayı temsil eden bir model bulunamamıştır. Yüksek reaksiyon sıcaklığından ileri gelen sinterleşme ve cevherde bulunan trevorit mineralinin zor indirgenen yapısı bu çalışmada elde edilen en yüksek indirgenme derecesini %81 olarak sınırlandırmıştır.

2023, 39 sayfa

Anahtar Kelimeler: Direkt indirgeme, Laterit, Ferronikel, Akışkan yatak, Reaksiyon kinetiği

PREFACE AND ACKNOWLEDGEMENTS

I would like to express my deepest thanks to my esteemed advisor Associate Professor Dr. Nesibe DİLMAÇ for her great efforts and patience. Also, I would like to thank to Associate Professor Dr. Ömer Faruk DİLMAÇ for his technical assistance. Finally, I would like to thank my beloved family who have been by my side in every moment of my life for their patience, sacrifice and support.

Bashar MOHAMMED MOHAMMED JABER ALSABAK
Çankırı-2023

CONTENTS

LIST OF SYMBOLS

α	Reduction Degree or Reaction Extend (-)
ρ_g	Density of the Fluidizing Gas (kg/m^3)
ρ_s	Density of the Fluidized Solid (kg/m^3)
μ_g	Viscosity of the Fluidizing Gas (kg/m.s)
$\dot{Q}_{mf}$	Volumetric Minimum Fluidization Rate (m^3/s)
A	Arrhenius Frequency Factor (l $^{n-1}$. mol $^{1-n}$. s^{-1})
A_r	Cross Sectional Area of Fluidized Bed Reactor (m^2)
C	Concentration of Reducing Gas (mol/l)
d_p	Mean Diameter of Solid Particles (m)
E_a	Activation Energy (kJ/mol)
f(α)	Differantial Model Equation (-)
g	Acceleration Due to Gravity (9,81 m/s^2)
g(α)	Integral Model Equation (-)
k(T)	Rate Constant (l $^{n-1}$. mol $^{1-n}$. s^{-1})
m_0	Mass of the Fully Oxidized Ore (kg)
m_t	Instantaneous Mass of the Ore (kg)
m_r	Mass of the Fully Reduced Ore (kg)
n	Order of the Recation According to the Gas Reactant (-)
R	Universal Gas Constant (8,314 J/mol.K)
T	Absolute Temperature (K)

LIST OF ABBREVIATIONS

MFC	Mass Flow Controller
PLC	Programmable Logic Controller
SEM	Scanning Electron Microscope
XRD	X-Ray Diffractometry
XRF	X-Ray Fluorescence Spectroscopy

LIST OF FIGURES

LIST OF TABLES

1. INTRODUCTION

1.1 Nickel

Nickel (Ni) is a silvery-white, lustrous, and ferromagnetic metal which melts at 1455 ºC and boils at 2913 ºC. It is the fifth most abundant element on our planet, and it belongs to the transition metals family (Figure 1.1). It was first identified and isolated as an element by the Swedish chemist Axel Cronstedt in 1751 (NICKEL INSTITUTE 2023). Since it reacts with oxygen, it is rarely found as a pure metal in nature, but in stable compounds, mostly in combination with sulfur and iron. Although it is a relatively low conductor of electricity and heat, it increases strength and resistance to corrosion when it is alloyed with other metals such as iron, silver, and chromium. It is highly ductile and also has fine catalytic properties.

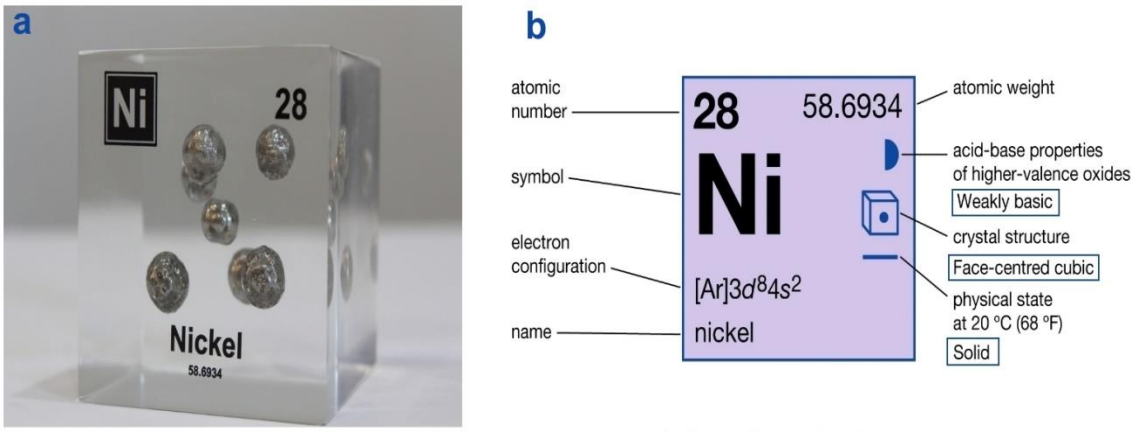

Figure 1.1 Ni element and its main properties a) ETSY 2023 b) BRITANNICA 2023

As seen in Figure 1.2, about 65% of nickel is consumed in the manufacturing of austenitic stainless steel and heat-resistant steel for construction, while 12% goes into superalloys which are essential for combustion turbines and aerospace engineering, and the remaining is utilized in batteries, coinage, foundry and military, marine, transportation industries. So the demand for it is great, and it is constantly growing (Yang *et al.* 2016, Elliott and Pickles 2017, Wang *et al.* 2017, Lv *et al.* 2018, Li *et al.* 2018, Zhu *et al.* 2019, Zhang *et al.* 2020).

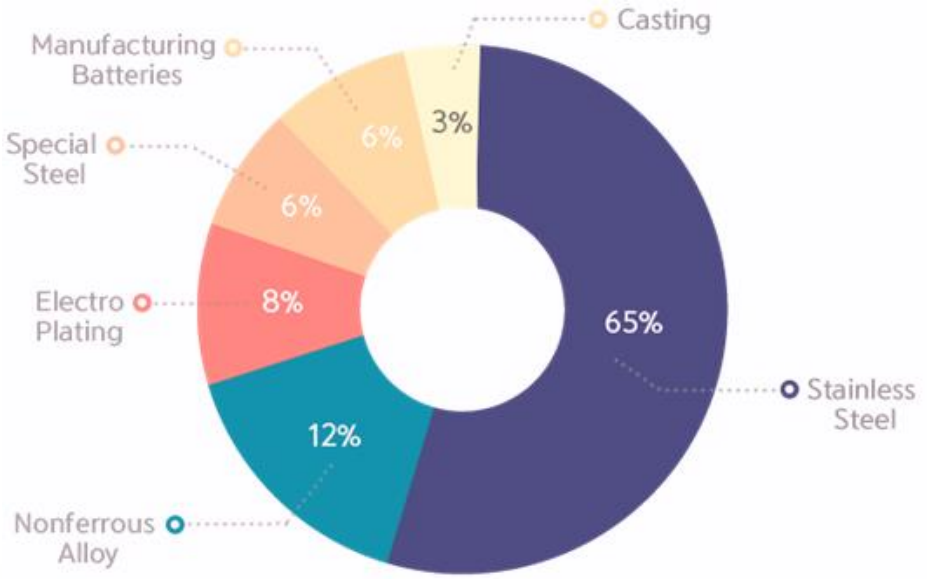

Figure 1.2 Main utilization areas of nickel (INSIDEXPLORATION 2023)

Nickel is available as ores in the form of sulphides and oxides. The global nickel resources are currently estimated as approximately 300 million tons as seen in Figure 1.3. Sulphide deposits are mainly distributed in South Africa, Canada, Russia, and Australia (Zhou 2005), while laterites primarily take place in South-East Asia.

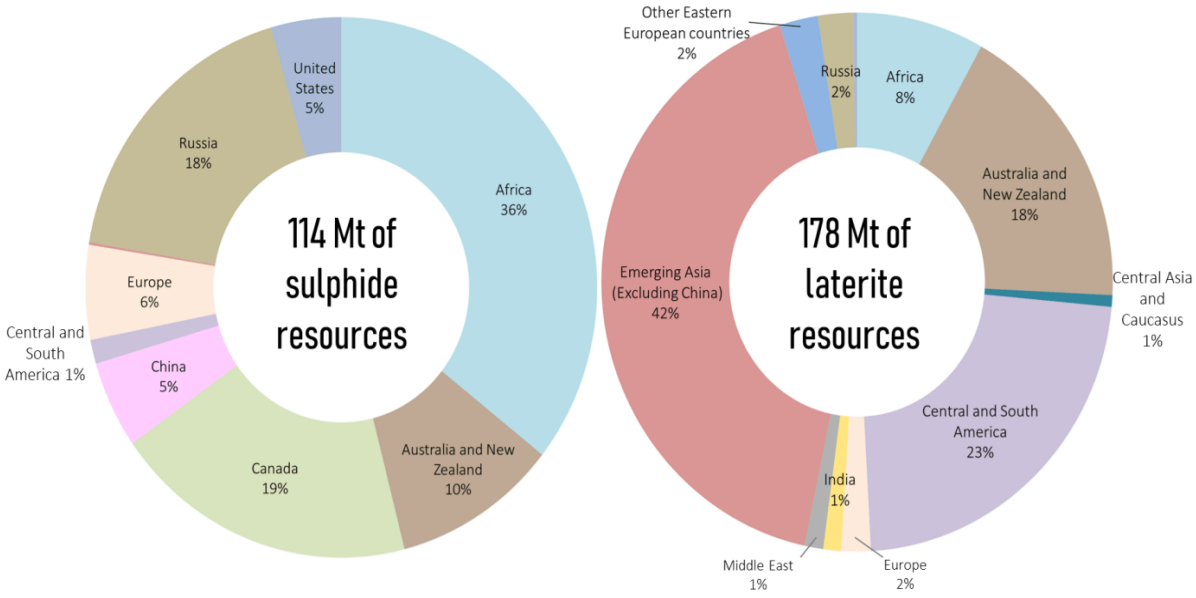

Figure 1.3 Global nickel resources (IFP ENERGIES NOUVELLES 2023)

Because of the depleting sulphide reserves, which were the main source of nickel production in the past (Whittington and Muir 2000), the sector is turning to extracting nickel from laterite ores which includes about 70% of nickel resources and may greatly vary in mineralogy according to location, climate and depth (Valix *et al.* 2001, Zhai *et al.* 2009, Norgate and Jahanshahi 2011). Figure 1.4 illustrates the trend from sulphides to laterites in nickel mining between the years 1995 and 2010.

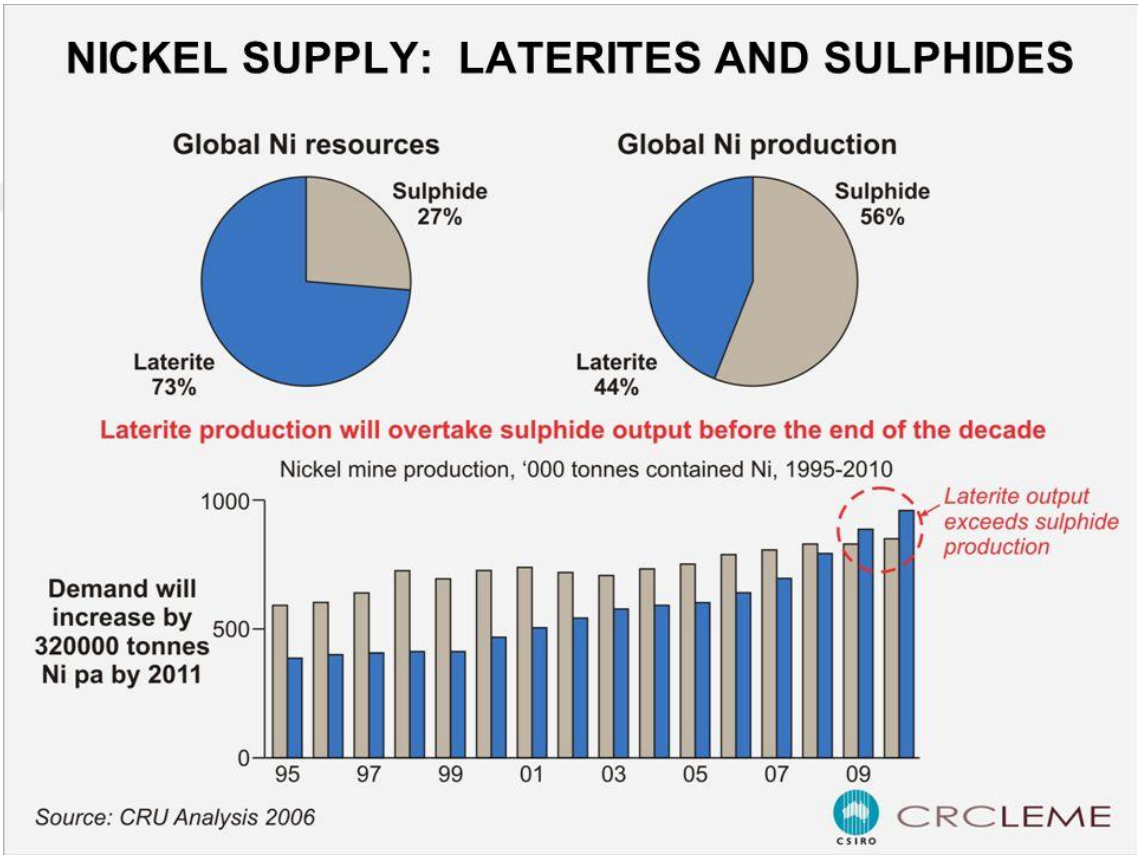

Figure 1.4 Trend from sulphides to laterites in Ni mining from 1995 to 2010 (SLIDESERVE 2023)

The largest nickel deposits in Turkey are located in the regions of Manisa-Turgutlu-Çaldağ, Manisa-Gördes and Eskişehir-Mihaliçcik-Yunus Emre (Figure 1.5). In Turkey, nickel has been mined by some private companies in recent years, and the total known nickel ore reserve is about 40 million tons, of which nearly 30 million tons are located in the Manisa-Çaldağ deposit (MTA 2018).

Figure 1.5 Ni deposits in Turkey (MTA 2023)

1.2 Nickel Production

The production process in Ni manufacturing highly depends on the type of ore. Sulphides are more labor-intensive to mine as they are generally found in deep underground, however the seperation stage for these ores is easier. Mostly flotation, magnetic separation, and hydrometallurgical methods are used for the extraction of nickel from these ores. Furthermore, they include other valuable elements as impurities.

On the other hand, the mining of the laterites is easier, but the seperation stage is more stringent. The metallurgical processes for extracting nickel from laterite ores include smelting the metal from the ore (pyrometallurgical method), leaching the metal from the ore (hydrometallurgical method), Caron process (a hybrid method), and a few new technologies such as chlorination and biological leaching (McDonald and Whittington 2008, USGS 2011). Since the composition of laterite varies according to the ore content and the physical properties of the sediment, nickel production technology is determined based on these properties. Table 1.1 and Figure 1.6 show typical laterite ore types and their processing techniques (Liu 2002).

Table 1.1 Processing technology for various laterite ores (Liu 2002)

Ore type	Chemical composition %					Processing technology
	Ni	Co	Fe	Cr_2O_3	MgO	
Limonite	0.8-1.5	0.1-0.2	40-50	2-5	0.5-5	Hydro
	1.5-1.8	0.02-0.1	25-40	1-2	1-15	Pyro or Hydro
Saprolite	1.8-3	0.02-0.1	10-25	1-2	15-35	Pyro

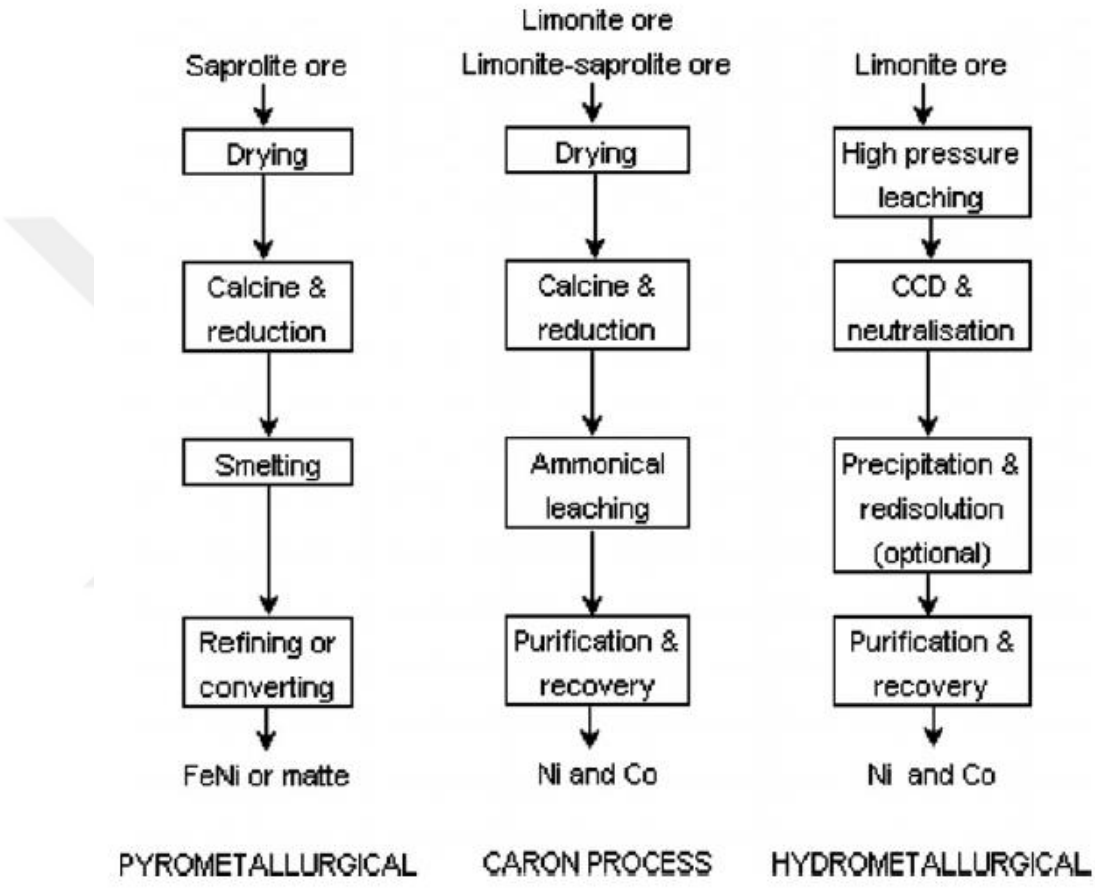

Figure 1.6 Main Ni production processes from laterites (Norgate and Jahanshahi 2011)

Figure 1.7 and Figure 1.8 show the world nickel production in 2020, and the variation of the estimated nickel demand by sector up to 2040, respectively. Besides being one of the most widely used metals (in over than 300.000 different products), the rapid development of the new generation transportation and energy storage industries has led to the sharp increase on nickel demand on recent years. As the major cathode material in lithium ion batteries used to power the electric vehicles (EVs), nickel is likely to play a vital role in the low-carbon future of our planet.

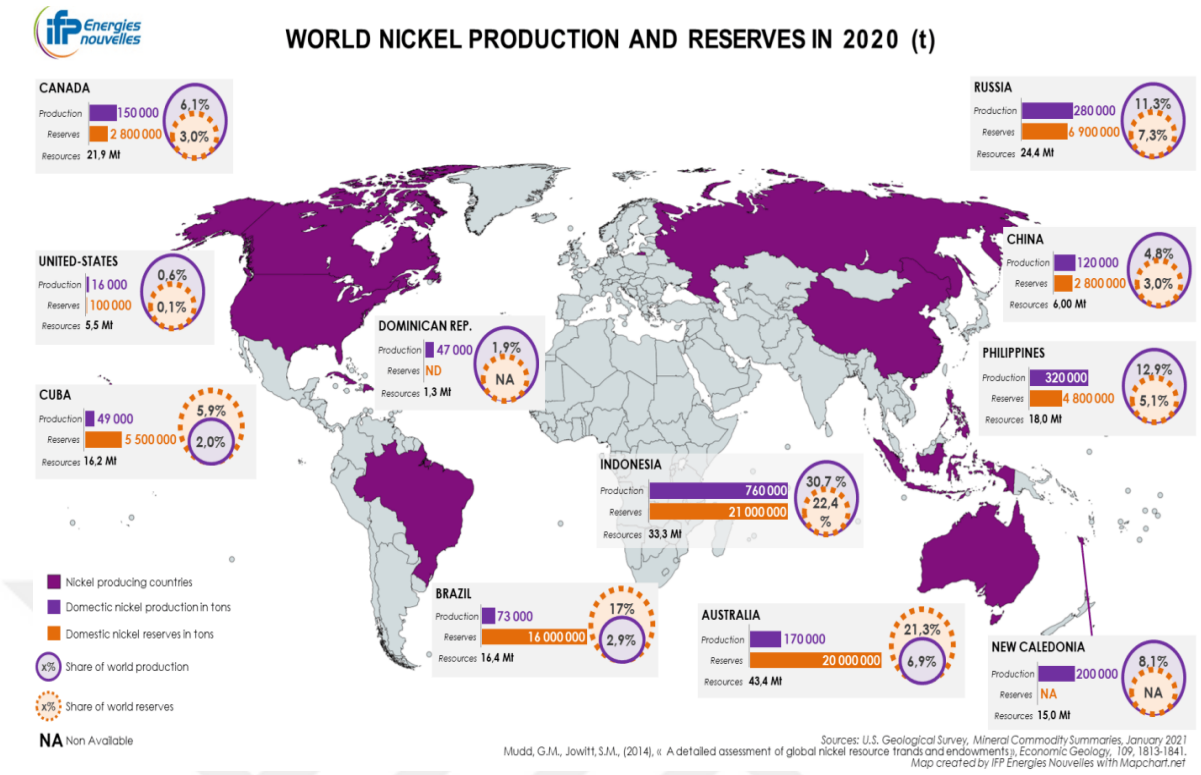

Figure 1.7 World nickel production in 2020 (IFP ENERGIES NOUVELLES 2023)

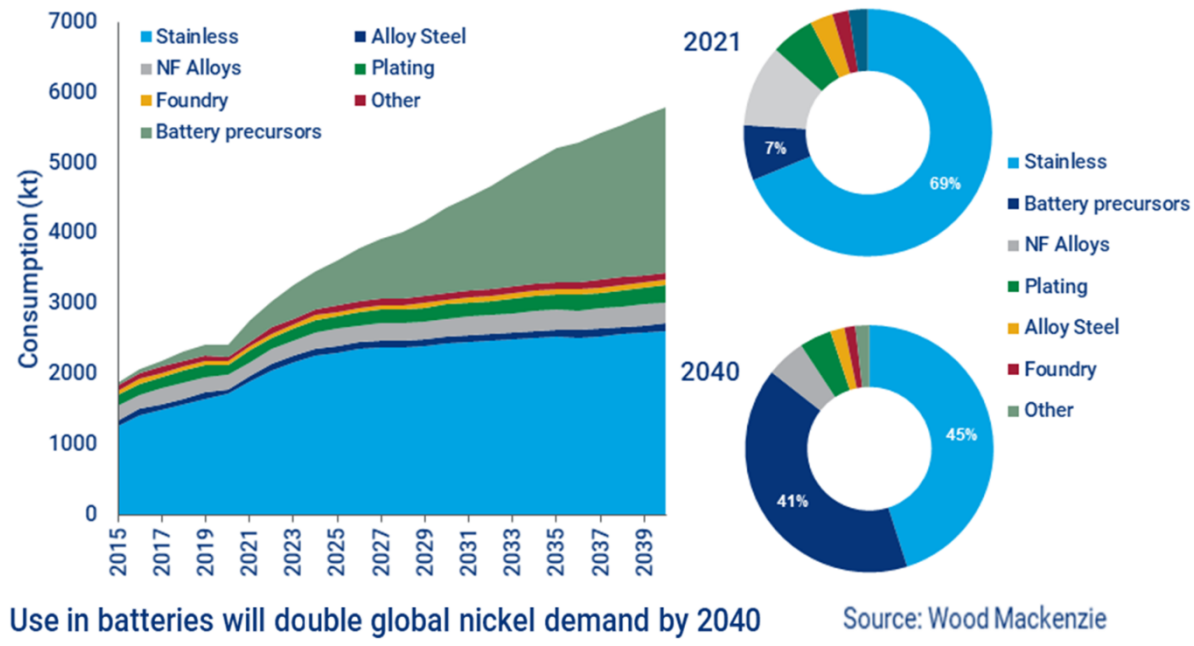

Figure 1.8 The variation of the estimated nickel demand by sector up to 2040 (WOODMAC 2023)

1.3 Gas-Solid Reaction Kinetics

The reduction of laterite follows the sequence given in Equation (1.1) to Equation (1.4) (Dilmaç 2021a).

$$3NiFe_2O_4 \rightarrow 3\text{NiO} + 3Fe_2O_3 \quad (1.1)$$

$$3\text{NiO} + 3Fe_2O_3 + 4H_2 \rightarrow 3Ni + 2Fe_3O_4 + 4H_2O \quad (1.2)$$

$$2Fe_3O_4 + 2H_2 \rightarrow 6FeO + 2H_2O \quad (1.3)$$

$$6FeO + 6H_2 \rightarrow 6Fe + 6H_2O \quad (1.4)$$

The conversion or reduction degree (α) of the metal oxides (iron and nickel oxides) forming the solid phase at any “t” moment of the reduction can be calculated with the help of Equation (1.5).

$$\alpha = \frac{m_o - m_t}{m_o - m_r} \quad (1.5)$$

In this equation, "m_o" is the mass of the ore in the fully oxidized state, "m_t" is the mass of the ore at any time "t", "m_r" is the mass of the ore in the fully reduced state (Dilmaç 2021b, AlSalihi 2022).

As is known, the rate (dα/dt) of any gas-solid reaction is expressed by Equation (1.6) (Su *et al*. 2017, Farooqui *et al.* 2018, Fedunik-Hofman *et al.* 2019).

$$\frac{d\alpha}{dt} = k(T).f(\alpha).C^n \quad (1.6)$$

In this equation, "k(T)" is the temperature dependent reaction rate constant, "f(α)" is the differential model function describing the reaction mechanism, "C" is the concentration of gas reactant, and "n" is the order of the reaction relative to the gaseous reactant. If Equation (1.6) is rearranged and integrated, Equation (1.7) is obtained.

$$g(\alpha) = \int_0^{\alpha} \frac{d\alpha}{f(\alpha)} = \int_0^{t} k(T) \,.\, C^n \,.\, dt \qquad (1.7)$$

The "g(α)" seen in the above equation is the integral model function describing the reaction mechanism. Since "k(T)" has a constant value for experiments performed under isothermal conditions, the analytical solution of the above equation can be easily done. For this purpose, if the expression "$k(T).C^n$" is redefined as in Equation (1.8) and integrated by substituting it in Equation (1.7), Equation (1.9) is obtained.

$$k_i = k(T).C^n \qquad (1.8)$$

$$g(\alpha) = k_i.t \qquad (1.9)$$

Equation (1.9) is a very useful equation to elucidate the reaction mechanism. Namely, the equation representing the "t-g(α)" data of the reaction with the highest linear regression coefficient (R^2) among the various g(α) functions seen in Table 1.2 is the integral model function of the reaction. The slope of the resulting line is the "k_i" value of the reaction for the temperature and gas concentration at which the experiments are carried out.

If the above procedure is repeated for different gas concentrations at the same temperature, "C-k_i" pairs are obtained for the number of different concentrations studied. If these data are converted into "lnC-lnk_i" pairs and subjected to linear regression according to Equation (1.10), the slope of the drawn line gives the order of the reaction with respect to the gas reactant (n), and the interception gives the reaction rate constant at the working temperature (ln(k(T))).

$$\ln(k_i) = \ln(k(T)) + n.lnC \quad (1.10)$$

If the procedure up to this point is repeated for different temperatures, "T-ln(k(T))" pairs are obtained as the number of temperatures studied. If these data are converted into "1/T-ln(k(T))" pairs and subjected to linear regression according to Arrhenius equation given in Equation (1.11) , the slope of the drawn line gives the activation energy of the reaction ($-E_a/RT$) and the interception gives the frequency factor (lnA).

$$\ln(k(T)) = \ln\left(A.e^{\frac{E_a}{R.T}}\right) = \ln A - \frac{E_a}{R.T} \quad (1.11)$$

Table 1.2 The most common f(α) and g(α) functions for gas-solid reactions

Reaction Model	**Symbol**	**f(α)=(1/k_i).(dα/dt)**	**g(α)=k_i.t**
One-dimensional diffusion model	$D_1(\alpha)$	$1/(2\alpha)$	α^2
Two-dimensional diffusion model	$D_2(\alpha)$	$(-\ln(1-\alpha))^{-1}$	$(1-\alpha)\ln(1-\alpha)+\alpha$
Three-dimensional diffusion model (Jander equation)	$D_3(\alpha)$	$(3/2)(1-\alpha)^{2/3}(1-(1-\alpha)^{1/3})$	$(1-(1-\alpha)^{1/3})^2$
Three-dimensional diffusion model (Ginstein-Brounshtein equation)	$D_4(\alpha)$	$(3/2)((1-\alpha)^{-1/3}-1)$	$(1-2\alpha/3)-(1-\alpha)^{2/3}$
Chemical reaction controlled model (infinite plate)	$F_0(\alpha)$	1	α
Random nucleation model	$F_1(\alpha)$	1-α	-ln(1-α)
Chemical reaction controlled model (shrinking cylinder)	$R_2(\alpha)$	$2(1-\alpha)^{1/2}$	$1-(1-\alpha)^{1/2}$
Chemical reaction controlled model (shrinking sphere)	$R_3(\alpha)$	$3(1-\alpha)^{2/3}$	$1-(1-\alpha)^{1/3}$
Two-dimensional nuclei growth model (Avrami-Erofe'ev (m=2) equation)	$A_2(\alpha)$	$2(1-\alpha)(-\ln(1-\alpha))^{1/2}$	$(-\ln(1-\alpha))^{½}$
Three-dimensional nuclei growth model (Avrami-Erofe'ev (m=3) equation)	$A_3(\alpha)$	$3(1-\alpha)(-\ln(1-\alpha))^{2/3}$	$(-\ln(1-\alpha))^{1/3}$

1.4 Aim of the Study

Nickel is expected to be of great value in future societies, and the nickel industry will continue to grow steadily (MTA 2018). While stainless steel will continue to be the main first consumer of the nickel metal, the major engine of demand growth over the next two decades will be the batteries, especially the electric vehicles (WOODMAC 2023). It is expected that battery precursor manufacturing will be responsible from 40% of the global nickel consumption by 2040 (the share has been only 7% of the total market in 2021). That will push nickel demand to double in size to 6 million tonnes per year.

Since the sulphide deposits are being depleted, it is essential to find new ways to extract nickel from lateritic ores. This thesis is performed within the scope of this motivation. It aimed to carry the advantages of direct reduction technology that was being used in steel industry for years for sponge iron manufacturing, in to ferronickel manufacturing area.

2. LITERATURE REVIEW

Extraction of nickel from laterites has attracted attention since 1867 when the rich nickel silicate deposits of New Caledonia were discovered (Li 1999).

Szekely and Evans (1970) proposed a "grain model" for kinetic analysis of NiO reduction based on the assumption that a porous particle consists of a large number of identical and topochemically reduced and densely structured spherical subunits, namely grains. The model defines units ranging in size from 1-50 μm as "grains", and those ranging in size from 1-50 mm as "particles" and assumes that the particle size does not change as a result of a single reaction. The said model (Evans *et al.* 1976), which was successfully applied to the reduction of NiO with hydrogen at temperatures below 620^{o}C, overestimated the reaction rate at temperatures above 620^{o}C, as it ignored the retarding effect of slowed diffusion.

Evans *et al.* (1976) reduced fine NiO particles with hydrogen and nitrogen mixtures with streams of 2-4 times the minimum fluidization rate in a temperature range of 550-650 K in a batch fluidized bed unit. They used the Szekely and Evans (1970) model for the kinetic analysis of their experimental data. The degree of progression of the reaction was determined by the weight gain method based on the retention of water formed as a result of reduction. The authors put forward that the best way to accurately determine the reaction rate constant for a gas-solid reaction is to set the experimental conditions so that only the chemical reaction controls the rate of the process. If the particle is sufficiently porous and its size is small enough, the diffusion resistance of the reactant and product gases through the pores will be weakened. In addition, the efficiency of the boundary layer resistance is reduced by allowing the reactant gas to pass around the particle at high speed. Keeping the reaction temperature low also increases the likelihood that the chemical reaction will control the rate of the process. Therefore, in the determination of the rate constant of the reduction reaction of NiO with H_2, Evans *et al.* (1976) preferred operating the fluidized bed at moderate temperatures and meeting the above-mentioned conditions. As a result of both thermal analysis and fluidized bed experiments, a linear relationship between time and conversion up to 90% progress was

observed, so it was concluded that the step controlling the reduction process was the chemical reaction.

Jankovic *et al.* (2007, 2008) reduced the synthetic nickel oxide (25 mg) prepared by sol-gel technique by non-isothermal way in a thermal gravimetric analyzer at 4 heating rates (2.5, 5, 10, and 20 ºC/min.) from ambient temperature to 1773 K (1500 ºC) under 100% H_2 atmosphere of 100 ml/min volumetric flow rate. They preferred FR, KAS, FWO, Kissinger, Stationary Point, and Invariant Kinetic Parameters methods for kinetic analysis of the obtained data. They obtained almost stable activation energy of 90 kJ/mol for the entire process from beginning to end. They depended this situation into the high purity of material. Since no other metal oxides such as iron oxide, took place in the solid structure, the reduction did not take include multisteps manner and fort his reason activation energy remained almost constant. For further analysis, Malek interpretation of Sestak-Berggren method was used and as can be estimated a single step reduction was determined.

Lv *et al.,* (2017) non-isothermally reduced the calcined laterite ore from Philippines (20 mg with 1.81% Ni and 17.87% Fe) using high purity carbon powder at 3 heating rates (10, 15 and 20 ºC/min.) from ambient temperature to 1773 K (1500 ºC) in a thermal gravimetric analyzer under Ar atmosphere. The authors determined that the reduction path may be divided in to 3 stages according to the conversion level $\alpha = 0 - 0.40$, $\alpha = 0.40 - 0.70$, and $\alpha = 0.70 - 0.9$ with mean "E_a" values of 60 kJ/mol, 137 kJ/mol, and 383 kJ/mol, respectively. The first stage was chemical reaction controlled while the knowledge about the second and third stages was inadequate for Masterplot interpretation.

By using the same ore, Lv *et al.* (2018) repeated the above mentioned reduction process by graphite at the same experimental conditions. They used KAS method for kinetic analysis and monitored highly variable activation energy throughout the reduction which implies multistep reduction. Depending on the "$d\alpha/dt$ vs α" graph the reduction process was divided into 3 stages according to the conversion as low, medium and advanced reduction levels Each stage was analyzed by Coats-Redfern method for

further kinetic data. It was determined that first and second stages were diffusion controlled but last stage was chemical reaction controlled.

Dilmaç (2021b), investigated the non-isothermal reduction kinetics of Gördes laterite by CO in a thermal gravimetric analyzer at 5 heating rates of 20, 25, 30, 35, and 45 ºC/min. Friedman (FR), Kissinger-Akahira-Sunose (KAS), and Flynn-Wall-Ozawa (FWO) methods were prefereed for determination of the activation energy, while Malek interpretation of the Sestak-Berggren Equation was utilized for determination of the controlling mechanisms. The author determined that the reduction path was divided into 3 stages. The activation energies and controlling mechanisms were obtained as 53 kJ/mol and chemical reaction control for the first stage which takes place between "0 to 0.16" reduction levels, while 126 kJ/mol and 379 kJ/mol under mixed control for the second and the third stages which take place between "0.16 to 0.45", and "0.45 to 0.7" conversion levels, respectively.

3. MATERIAL AND METHOD

3.1 Laterite Ore

The laterite ore samples used in this study were supplied from Gördes (Manisa, Türkiye) mine via Meta Nickel Cobalt Company (META NİKEL KOBALT A.Ş.). The coarse ore pieces were crushed in a jaw breaker and sieved using standard sieves. In experiments, the ore fraction with an average diameter of 0.2 mm was used. The ore samples were calcined at 900 ºC for 18 hours in a muffle furnace to improve their mechanical properties. In all experiments approximately 5 g calcined ore samples were used. The XRF chemical composition of the raw laterite ore is given in Table 3.1. It is worth to emphasize that the Fe_2O_3 and NiO composition of the calcined ore increased up to 46.50% and 3.51% respectively due to the losses during calcination process.

Table 3.1 Chemical composition of Gördes laterite ore

Fe_2O_3	Al_2O_3	SiO_2	NiO	CaO	Cr_2O_3	MgO	SO_3	Other
42.31	8.82	33.11	3.19	3.66	1.67	2.22	0.5	4.52

3.2 Experimental Set-up and Method

The direct reduction experiments within the scope of this study were carried out in the set-up shown in Figure 3.1.

In the experiments, a quartz pipe with a length of 120 cm and an inner diameter of 2.2 cm -with a porous diffuser in the middle-, was used as the fluidized bed reactor. The reactor, loaded with 5 g of calcined ore, was placed in a vertical tube furnace, then gas-tight inlet and outlet connections were made, and it was started to be heated under nitrogen flow up to reaction temperature.

Figure 3.1 Experimental set-up

For each experiment, an "experimental scenario" including the procedure (the inert gas flow rate during heating, the reduction temperature at which the experiment will take place, the composition and flow rate of the reactive gas, the reduction time, and the nitrogen flow rate during cooling) was submitted into the computer software. The

software regulated the gas flow to the reactor in accordance with the scenario by directing the flowmeters (Mass Flow Controller, MFC) over the automation and control unit (Programmable Logic Controller, PLC) seen in Figure 3.1. Thus, the calcined ore was heated under inert nitrogen flow until the target temperature, afterwards it was reduced isothermally with the reactive gas mixtures whose composition and flow rate are given in Table 3.2.

Table 3.2 Experimental conditions

Temperature / **Composition**	**700 ºC**	**750 ºC**	**800 ºC**	**850 ºC**
10% H_2 + 90% N_2	706 (mL/min.)	652 (mL/min.)	603 (mL/min.)	570 (mL/min.)
25% H_2 + 75% N_2	774 (mL/min.)	714 (mL/min.)	661 (mL/min.)	614 (mL/min.)
40% H_2 + 60% N_2	856 (mL/min.)	790 (mL/min.)	731 (mL/min.)	679 (mL/min.)

As soon as the experiment was completed, the reactive gas flow and furnace heating were stopped and the cooling step was started. Meanwhile, nitrogen flow into the reactor was continued to prevent sticking of the reduced ore and to maintain fluidization. As the temperature of the reaction zone reached to the ambient temperature, the nitrogen flow was also cut off and the reactor was removed from the furnace, and the solid material in it was quickly transferred to a glass container.

The flow rates in Table 3.2 are 6 times the minimum fluidization rate ($\dot{Q}_{mf}$) calculated with the help of Equation (3.1) for each composition and temperature (Yang *et al.* 1985) where "d_p" is the mean diameter of ore (m), "ρ_s" is the density of ore (kg/m^3), "ρ_g" is the density of gas mixture (kg/m^3), "g" is acceleration due to gravity (9,81 m/s^2), "μ_g" is the kinematic viscosity of gas mixture (kg/m.s), and "A_r" is the cross sectional area of reactor (m^2).

$$\dot{Q}_{mf} = \frac{d_p^2.(\rho_s - \rho_g).g}{1650.\mu_g} \times A_r \quad (3.1)$$

3.3 Determination of Reduction Degree via Gas Analysis Data

During the experiments, the composition of the gas stream leaving the reactor (flue gas) was measured and recorded at 2-second intervals by the gas analyzer seen in Figure 3.1. For the reduction degree calculation, the "Time-Gas Composition" data from the gas analyzer were transferred to a column of a Microsoft Excel file. The difference between the inlet (which is 10%, 25%, or 40% as seen in Table 3.2) and outlet hydrogen concentrations is equal to the amount of the hydrogen consumed by the reduction reaction instantaneously. Thus, the total amount of hydrogen consumed from the beginning to the end of each experiment was determined by the help of Microsoft Excel. Then, the degree of reduction was calculated by proportioning the amount of the total consumed hydrogen to the theoretical amount for full reduction of ore (the hydrogen amount required to remove all the oxygen bound to the iron and nickel in the ore) as given in Equation (3.2).

$$Reduction\ Degree(\%) = \frac{(n_O)_{Amount\ of\ hydrogen\ consumed\ during\ test}}{(n_O)_{Amount\ of\ hydrogen\ required\ for\ full\ reduction}} \times 100 \quad (3.2)$$

The method described above, which is used to determine the progress of the reaction with the help of flue gas analysis, is quite common in the literature. However, since it is beyond the scope of this study to explain the method thoroughly, interested researchers can review the various studies for details (Dilmaç *et al.* 2012, Chen *et al.* 2017, Alsalihi 2022).

4. RESULTS AND DISCUSSION

4.1 Variation of Reduction Degree

The variation of the reduction degree of laterite samples was determined by using gas analysis data according to the method explained in Section 3.3. The obtained results for various temperatures and hydrogen concentrations were graphed as seen in Figure 4.1 and Figure 4.2, respectively.

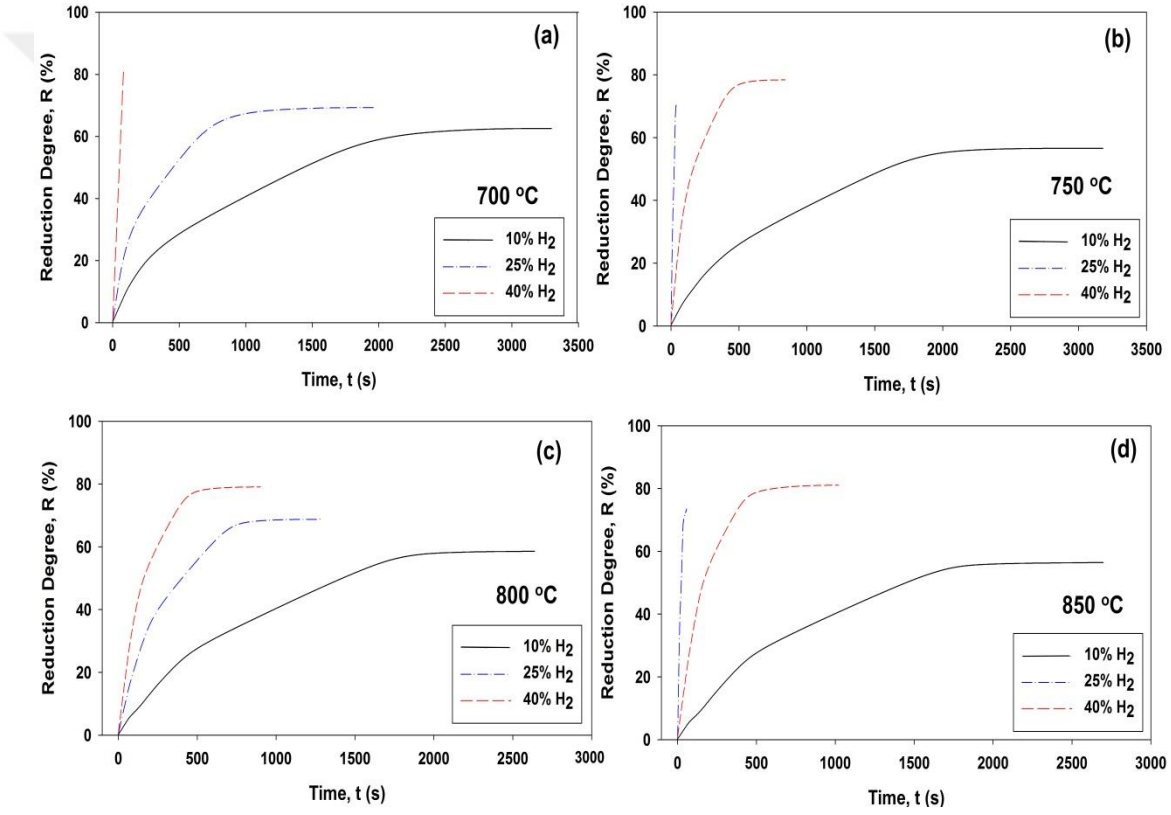

Figure 4.1 Effect of reaction temperature on the reduction degree

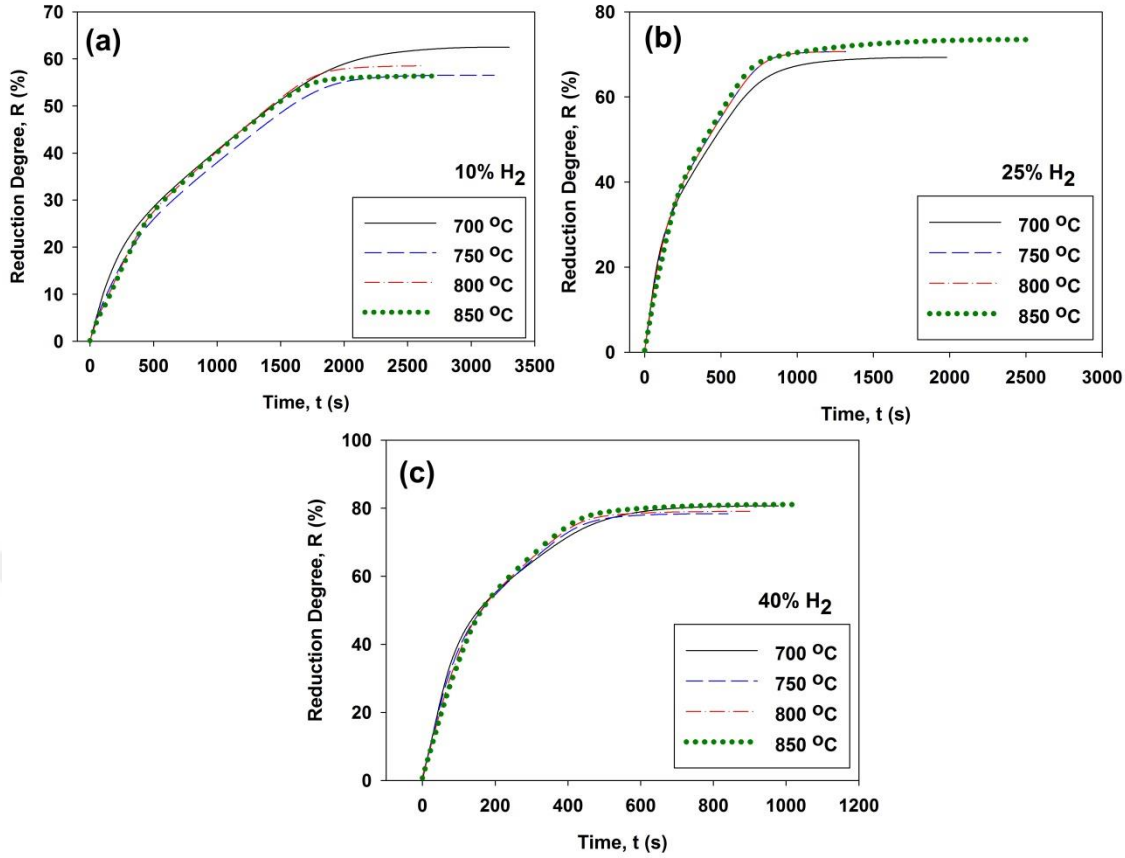

Figure 4.2 Effect of H2 concentrations on the reduction degree.

As seen in Figure 4.1 and Figure 4.2, the reduction behaviour of the laterite samples are more sensitive to H_2 concentration than the reaction temperature. This finding strengthens the argument that the reduction reaction took place mostly under diffusion control since the increase of the reaction temperature caused almost no increase in the conversion degree for a given H_2 concentration and reaction time. To verify this argument, kinetic analysis is performed in the following section.

4.2 Determination of Reduction Kinetics

To determine the reduction kinetics of calcined Gördes laterite by hydrogen, the "Time-Reduction Degree" data of all experiments seen in Figure 4.1 were converted into "t-g(α)" graphs for each reaction model in Table 1.2 via Microsoft Excel. A single model could not represent the entirety of the kinetic data from the beginning to the end of the

experiment with acceptably high linear regression coefficients (R^2), it was thought that it would be more accurate to divide the reaction path into different regions exhibiting similar reaction rates and to model each region within itself. As an example, Figure 4.3 shows how the kinetic data belonging to the experiment performed at 700 ºC with 10% H_2 was divided into 3 kinetic regions with different reaction rates. The same approach was adopted for all other experiments.

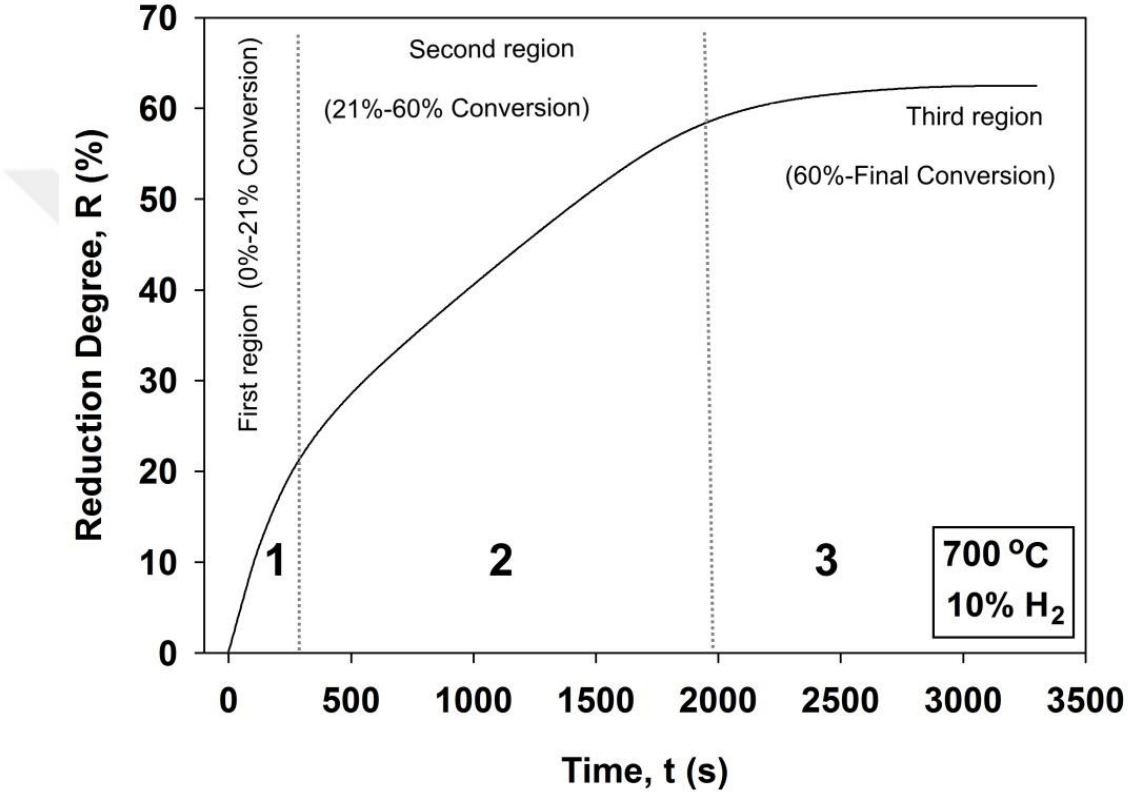

Figure 4.3 The way that kinetic data divided into 3 regions for modeling

4.2.1 Modeling of the first region

"Time-Reduction Degree" data belonging to the first region of all experiments were converted into "t-g(α)" graphs via Microsoft Excel according to the model equations given in Table 1.1. The graphs obtained according to Equation (1.9) were examined and it was seen that the "Contracting Sphere, R3(α)" model yielded highest linear regression coefficient (R^2) for all temperatures and hydrogen concentrations. Thus, it was

concluded that the first region of the H_2 reduction of calcined Gördes laterite in fluidized bed was driven under chemical reaction control.

The related graphs including regression analysis are given in Figure 4.4, Figure 4.5, Figure 4.6, and Figure 4.7 respectively. The slope of the lines are the "k_i" values for the first stage of the reduction at the test conditions according to Eq. (4.1).

$$g(\alpha) = 1 - (1 - \alpha)^{1/3} = k_i . t \qquad (4.1)$$

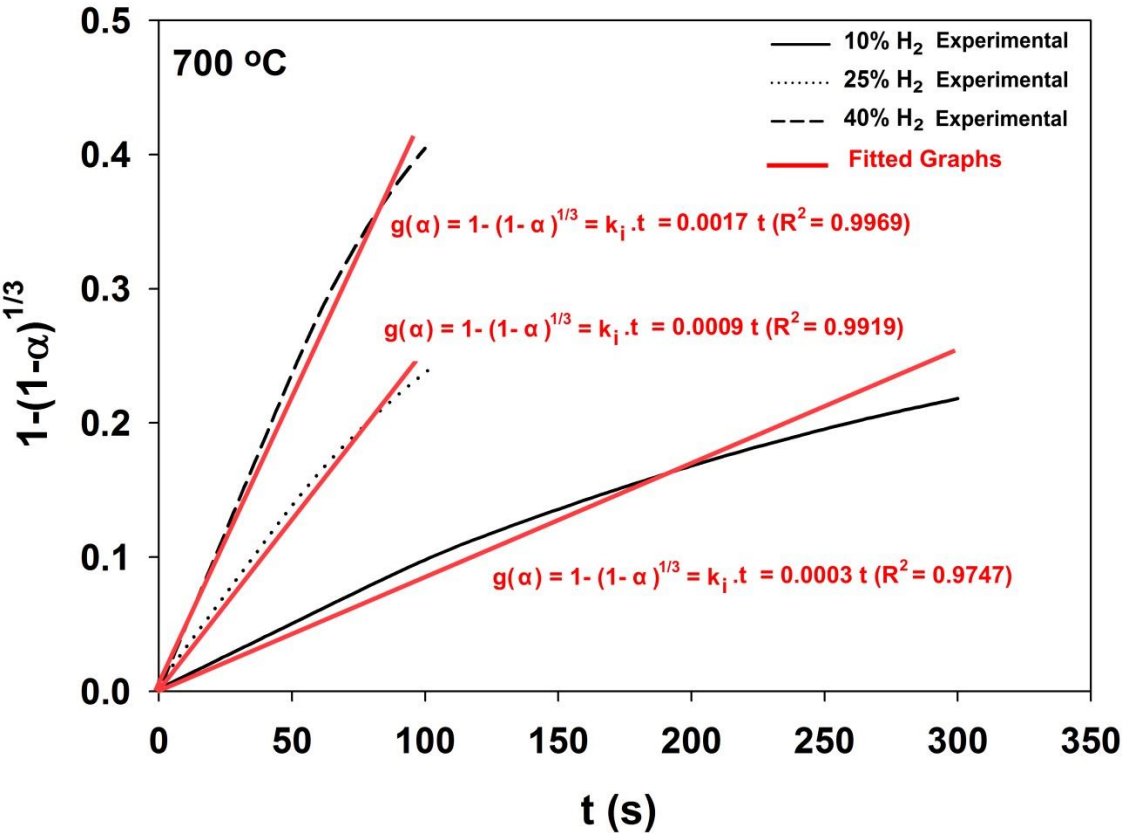

Figure 4.4 Modeling of the first stage of the reduction at 700 ºC

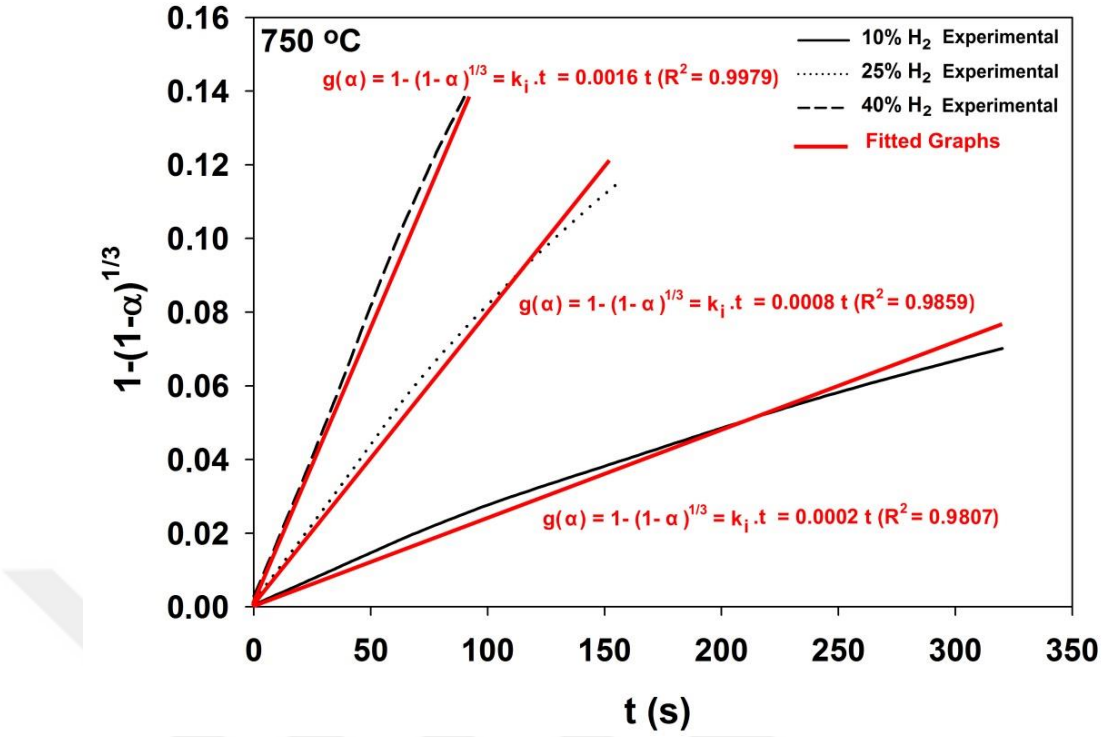

Figure 4.5 Modeling of the first stage of the reduction at 750 ºC

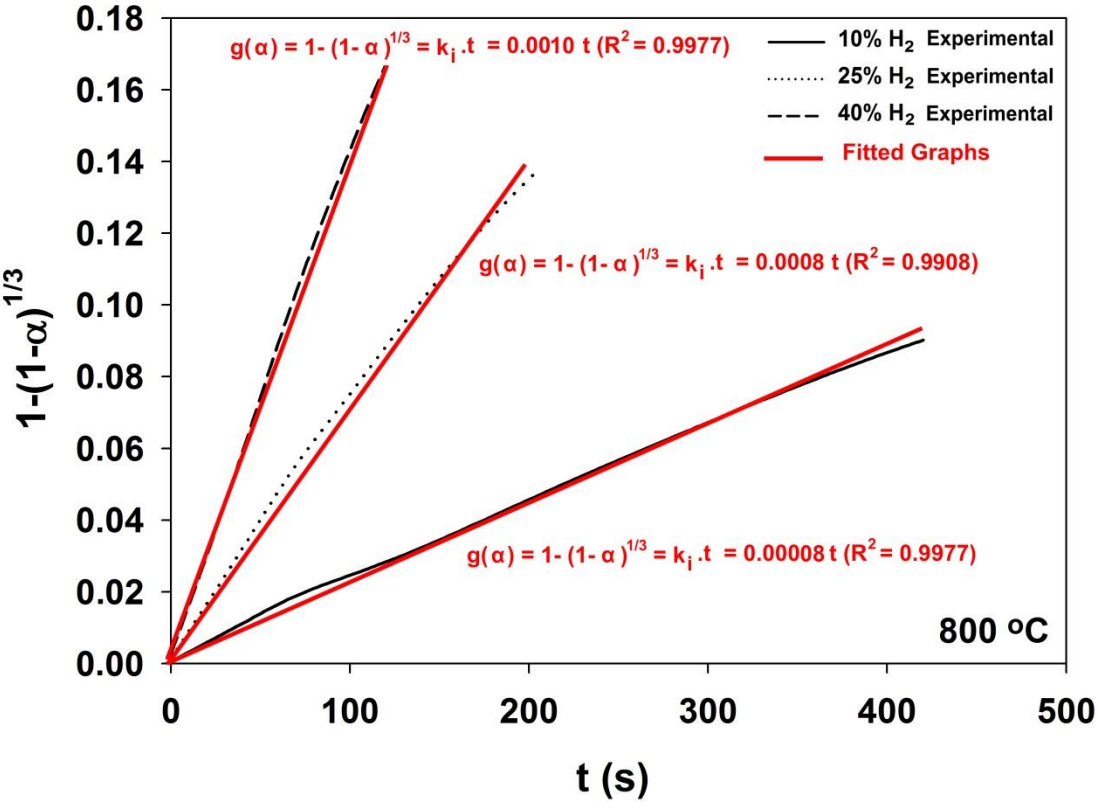

Figure 4.6 Modeling of the first stage of the reduction at 800 ºC

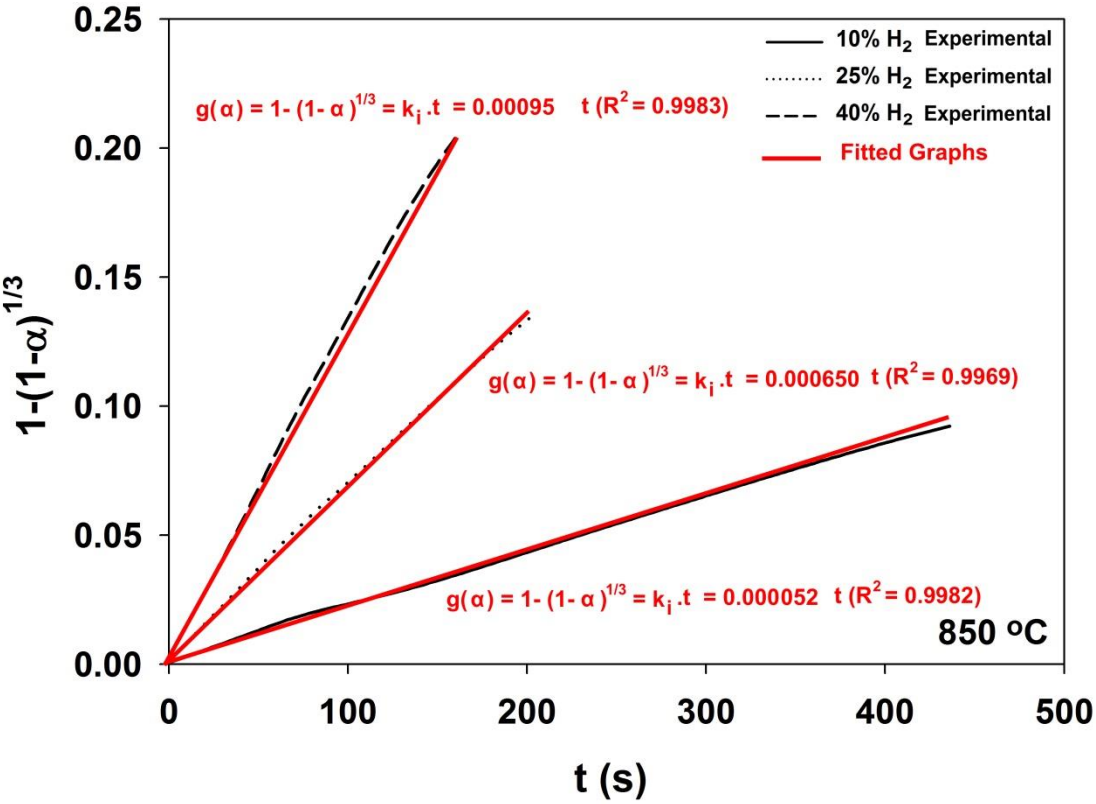

Figure 4.7 Modeling of the first stage of the reduction at 850 ºC

After determining the reaction model and the "k_i" values, a new linear regression procedure was performed using "lnC-lnk_i" data of each isothermal set according to Eq. (4.2), and the lines shown in Figure 4.8 were obtained. Thus, the order of the first stage of the reduction according to the H_2 concentration was determined as 1.7 as a mean of 4 temperatures.

$$\ln(k_i) = n.\ln\left(C_{H_2}\right) + \ln k(T) \qquad (4.2)$$

In the last step of the kinetic analysis, the intercept values of the lines seen in Figure 4.8 (lnk(T) values) were graphed against the reciprocal of the corresponding absolute temperatures (see Eq. (1.11)). As a result of the linear regression (Figure 4.9), the activation energy and the frequency factor for the first stage of the reduction was determined as 34.76 kJ/mol, and 0.3833 $l^{n-1}.mol^{1-n}.s^{-1}$, respectively.

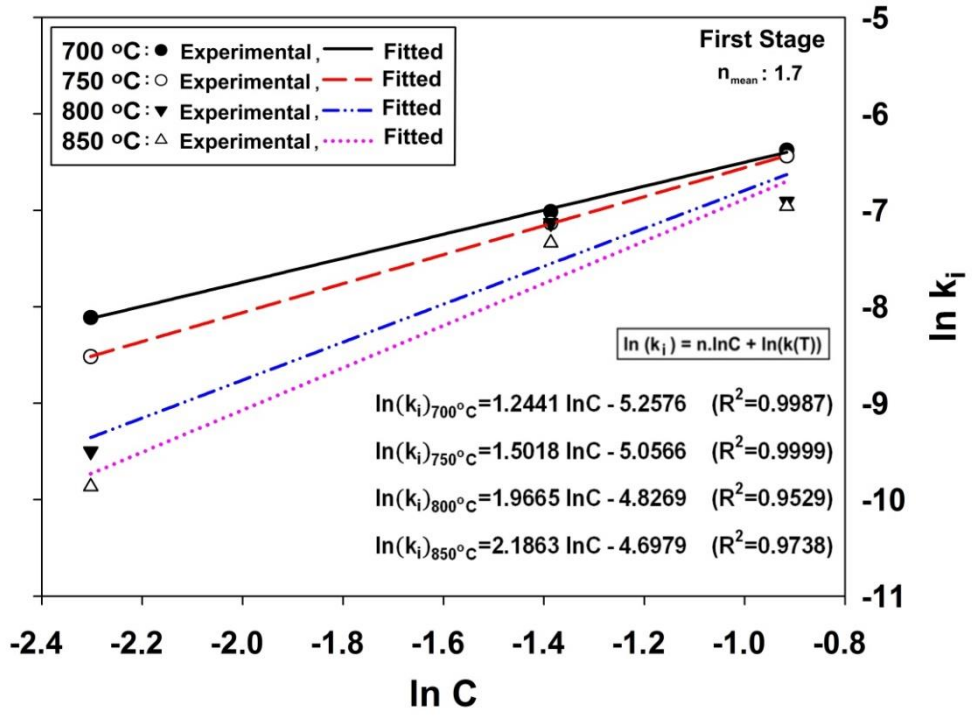

Figure 4.8 Determination of the order of the first stage of the reduction according to the H_2 concentration

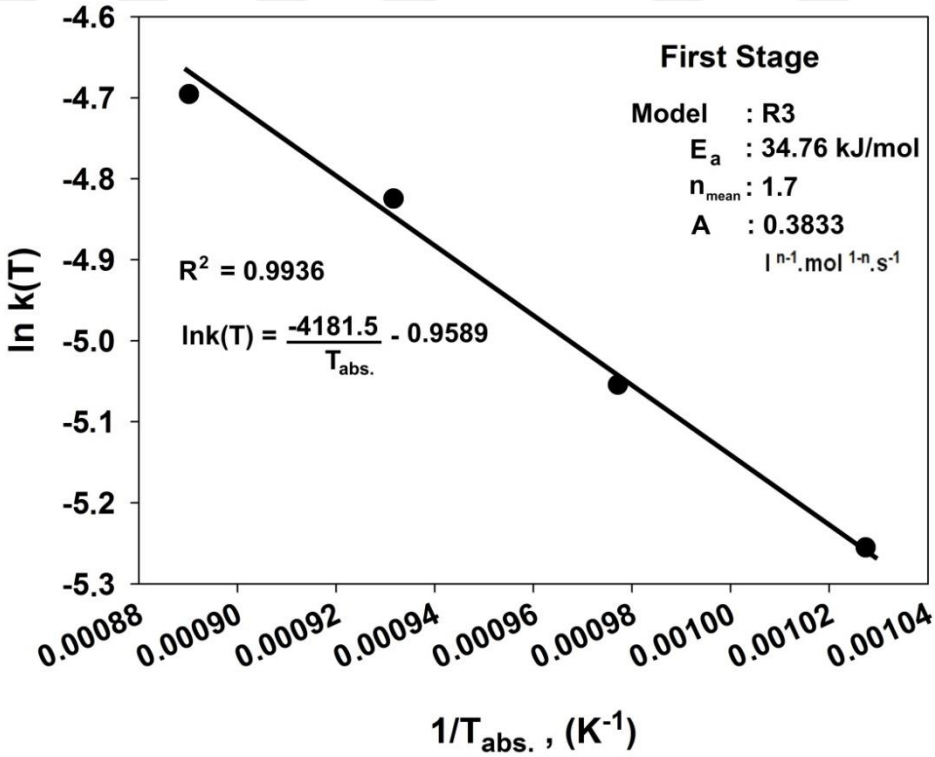

Figure 4.9 Determination of "E_a" and "A" values of the first stage of the reduction

4.2.2 Modeling of the second region

"Time-Reduction Degree" data belonging to the second region of all experiments were converted into "t-g(α)" graphs via Microsoft Excel according to the model equations given in Table 1.1. The obtained graphs were examined and it was seen that the "One Dimensional Diffusion, D1(α)" model yielded highest linear regression coefficient (R^2) for all temperatures and hydrogen concentrations. Thus, it was concluded that the second region of the H_2 reduction of calcined Gördes laterite in fluidized bed was driven under diffusion control.

The related graphs including regression analysis are given in Figure 4.10, Figure 4.11, Figure 4.12, and Figure 4.13 respectively. The slope of the lines are the "k_i" values for the second stage of the reduction at the test conditions according to Eq. (4.3).

$$g(\alpha) = \alpha^2 = k_i.t \tag{4.3}$$

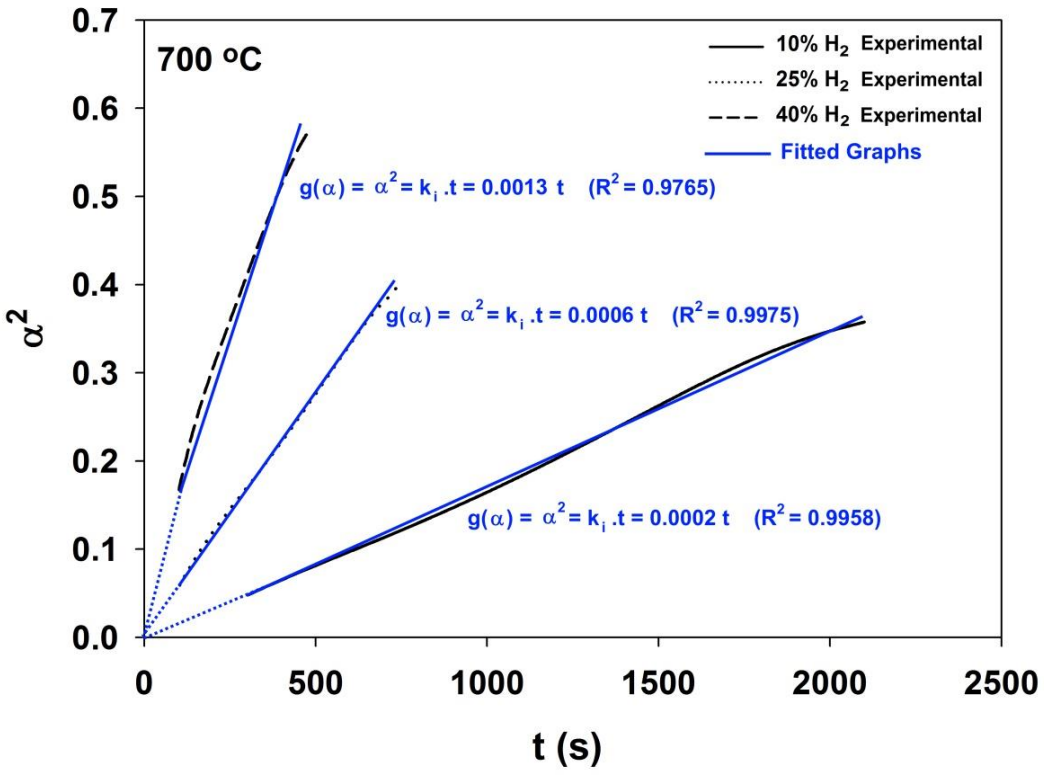

Figure 4.10 Modeling of the second stage of the reduction at 700 ºC

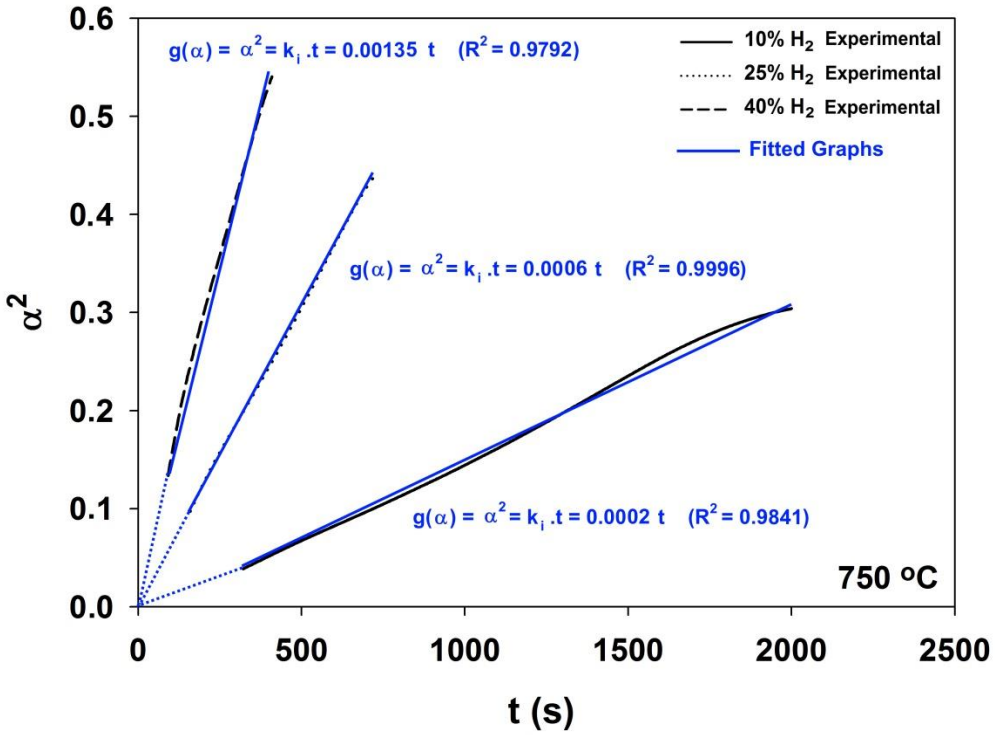

Figure 4.11 Modeling of the second stage of the reduction at 750 ºC

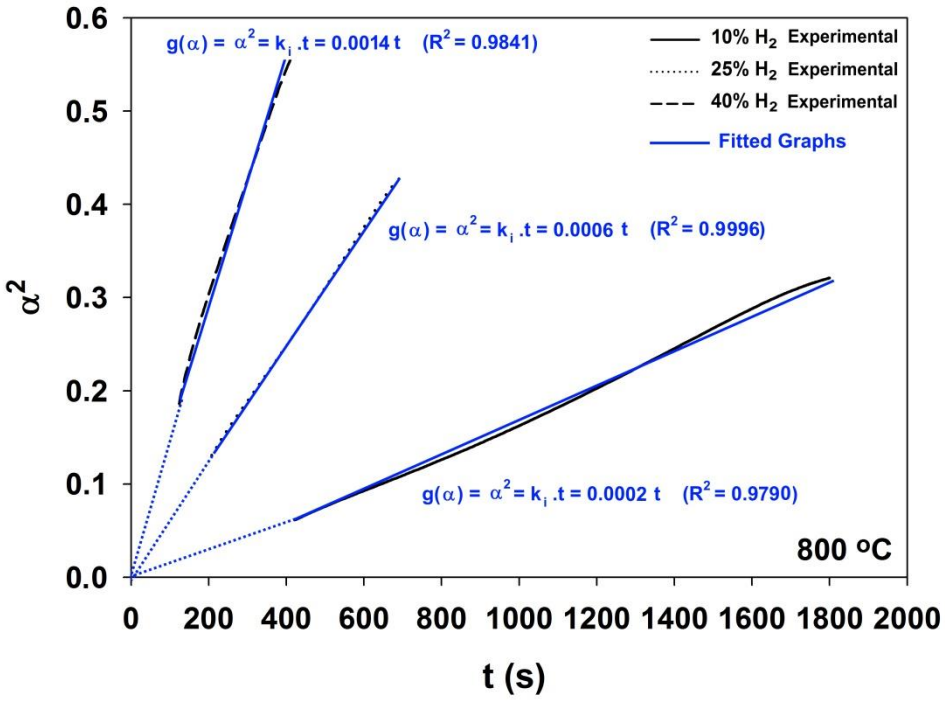

Figure 4.12 Modeling of the second stage of the reduction at 800 ºC

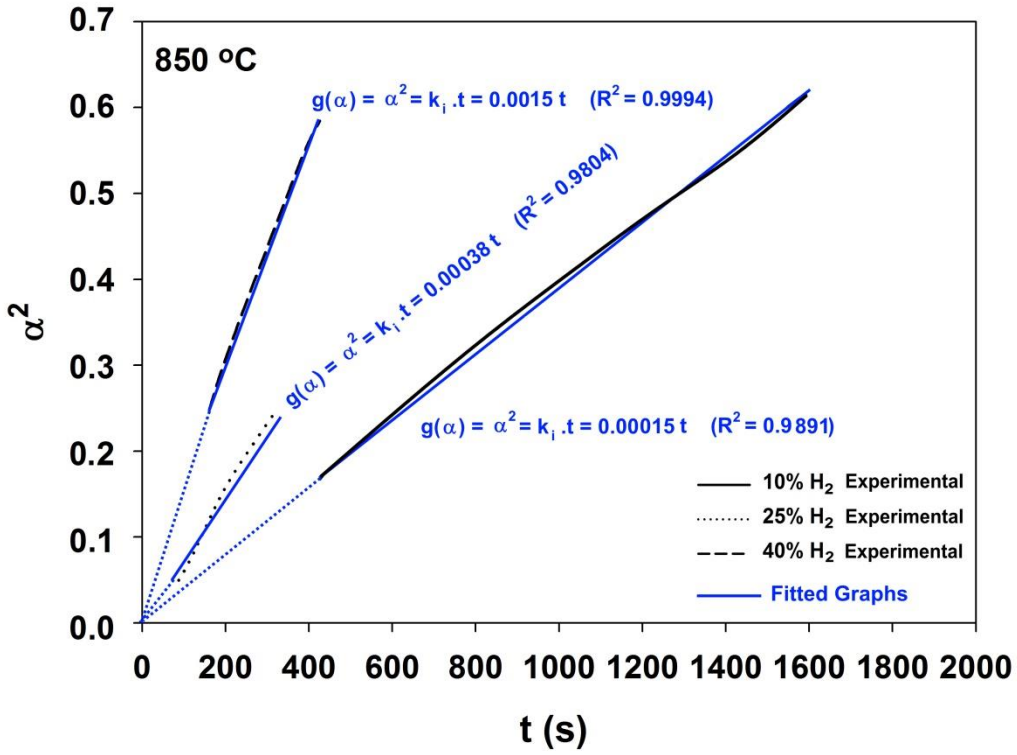

Figure 4.13 Modeling of the second stage of the reduction at 850 ºC

After determining the reaction model and the "k_i" values, a new linear regression procedure was performed using "lnC-lnk_i" data of each isothermal set, and the lines shown in Figure 4.14 were obtained. Thus, the order of the second stage of the reduction according to the H_2 concentration was determined as 1.4 as a mean of 4 temperatures.

In the last step of the kinetic analysis, the intercept values of the lines seen in Figure 4.14 (lnk(T) values) were graphed against the reciprocal of the corresponding absolute temperatures (see Eq. (1.11)). As a result of the linear regression (Figure 4.15), the activation energy and the frequency factor for the second stage of the reduction was determined as 10.18 kJ/mol, and 0.0145 $l^{n-1}.mol^{1-n}.s^{-1}$, respectively.

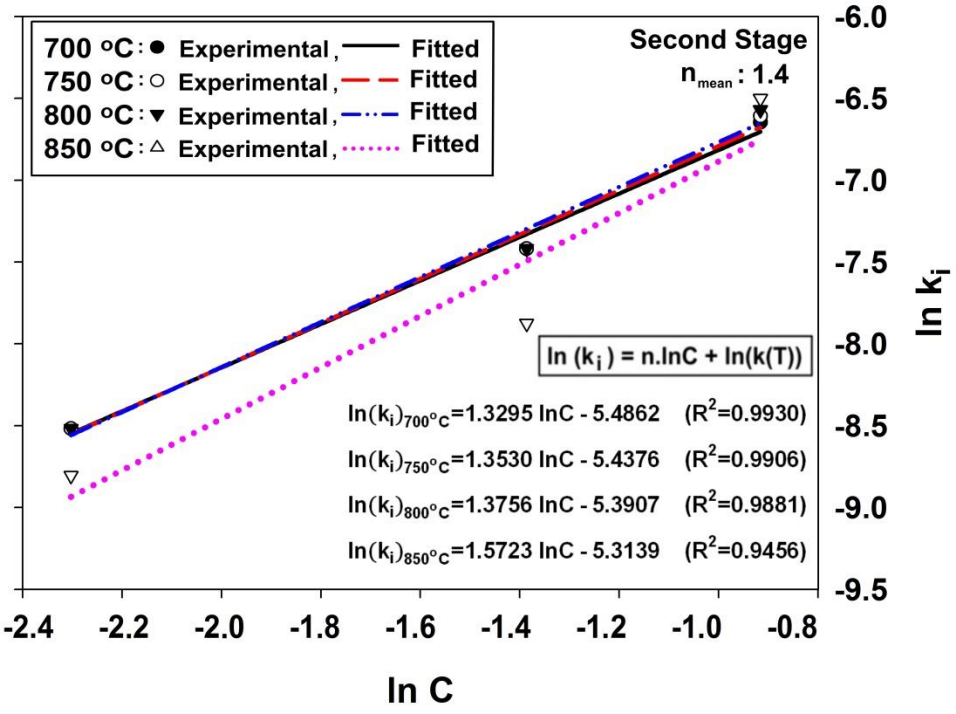

Figure 4.14 Determination of the order of the second stage of the reduction according to the H_2 concentration

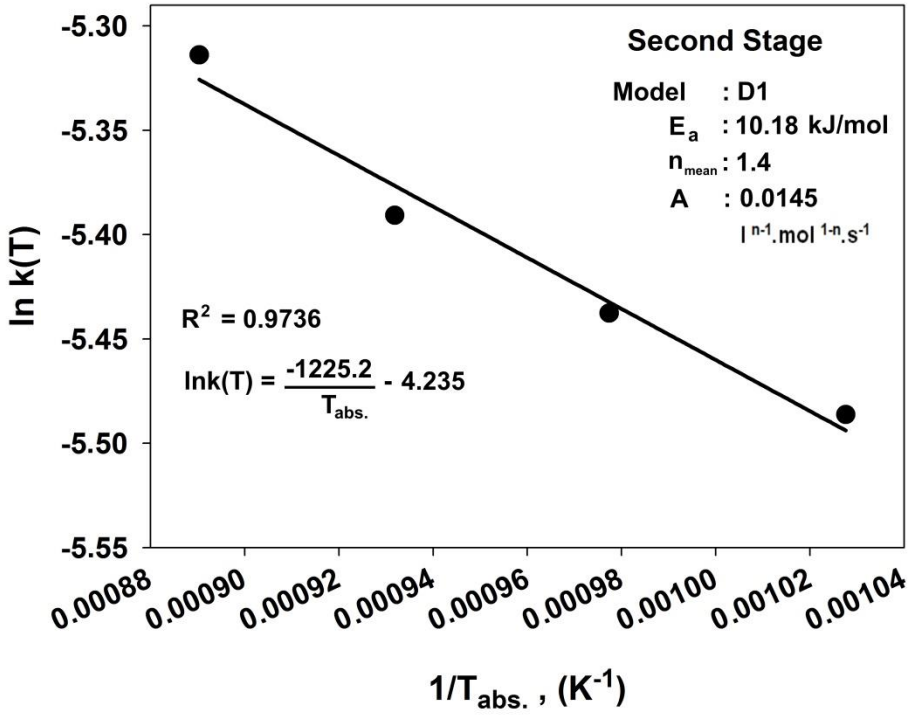

Figure 4.15 Determination of "E_a" and "A" values of the second stage of the reduction

4.2.3 Modeling of the third region

A model representing the kinetic data of the third stage could not be found. Moreover, it should be emphasized that, the reaction progress recorded at this stage corresponds to the last 2% or 3% of the final reduction degree. Thus, not modeling this stage caused almost no deficiency in terms of kinetic analysis in a practical view.

4.3 Characterization of the Reduced Samples

4.3.1 XRD analysis

The X-ray diffraction (XRD) analysis of the unprocessed ore and a number of reduced samples was performed via Panalytical Empyrean diffractometer, using CuKα radiation (40 kV, 100 mA) at a scanning rate of 4˚ per minute from 5˚ to 85˚. The obtained XRD patterns are given in Figure 4.16.

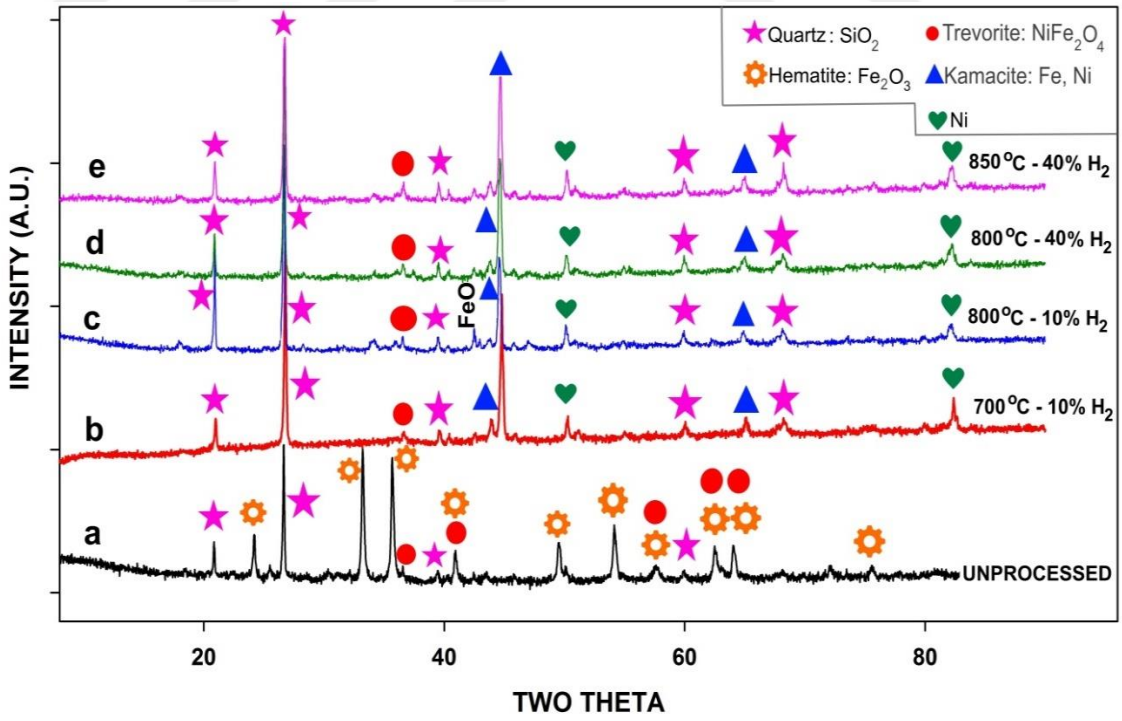

Figure 4.16 XRD patterns of a number of samples

XRD analysis clearly reveals the impact of the reduction process on the mineralogy of the ore. While the majority of the metal oxide peaks (all of the Fe_2O_3 peaks, and most of the $NiFe_2O_4$ peaks) seen in Figure 4.16.a disappeared in the patterns of the reduced samples, only a small amount of trevorite peaks remained in Figure 4.16.b, c, d, and e due to the low reducibility of trevorite compared to the hematite. This also explains why laterite ore could not be reduced by more than 81% in this study.

On the other hand, as a result of the reduction of metallic oxides in the laterite ore, new peaks showing the presence of Ni and Fe metals emerged as seen in Figure 4.16. b, c, d, and e. Besides, the quartz peaks are slightly intensified in the patterns of the reduced samples compared to the diffractogram of the unprocessed sample.

4.3.2 SEM analysis

The SEM images of the unprocessed ore and a number of reduced samples are given in Figure 4.17, Figure 4.18, Figure 4.19, and Figure 4.20, respectively. The brighter appearance of the processed samples, especially the highly reduced ones, confirms the formation of Ni and Fe metals.

As seen in the figures, the reduction process noticeably changed the microscopic structure of the samples. The test conditions, particularly the composition of the reducing gas, were very effective on the said change. For example, the dense and angular texture of the unprocessed ore seen in Figure 4.17 was almost preserved in the samples reduced with 10% H_2 (see Figure 4.18.a and Figure 4.19.a), whereas, the porosity fairly increased (see Figure 4.18.b, Figure 4.19.b, and Figure 4.20) in samples reduced with higher H_2 concentrations. However, the said increase i.e. the transformation of the structure into a spongy new form after reduction, was more effective in lower temperatures as seen in Figure 4.18.b (700 °C), because higher temperatures caused sintering *i.e.* loss of pores due to the melt closing of the smallest pore walls. Besides, the lower melting points of the freshly formed Ni and Fe metals (compared to the ore) exacerbated the sintering process and created a self-braking mechanism against the full reduction of ore, especially in tests performed at higher

temperatures. Figure 4.20, in which almost all grains are round shaped, is a typical example of this situation since reduction took place at 850 °C in this test.

To summarize, the increase of porosity due to high H_2 concentration was counterbalanced by the microscopic effects of the sintering in tests performed at high temperatures. That is why H_2 concentration was more effective on reduction degree than the temperature and why almost the same conversion was achieved in all experiments performed at the same hydrogen concentration, regardless of the temperature (see Figure 4.2).

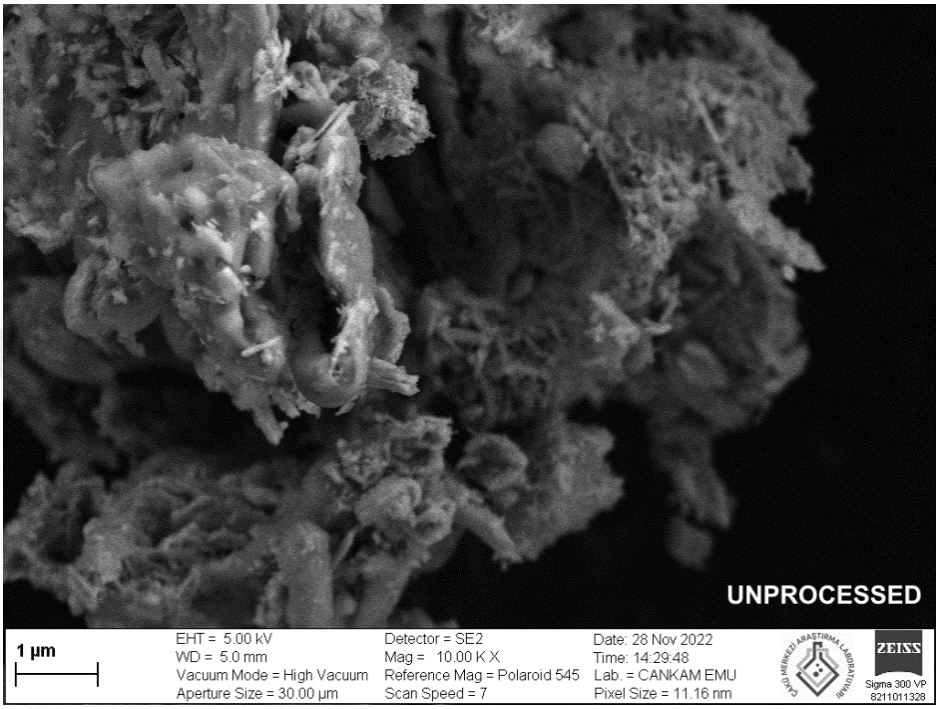

Figure 4.17 SEM image of unprocessed laterite ore (Magnification ×10000)

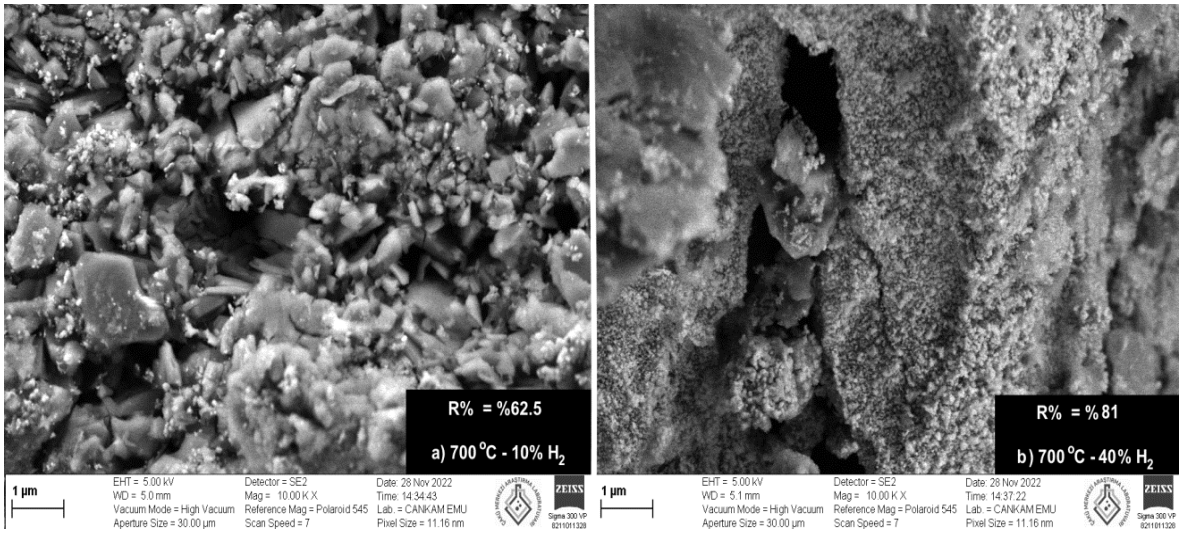

Figure 4.18 SEM images of the samples reduced at 700 ˚C by a) 10% H_2, b) 40% H_2 (Magnification ×10000)

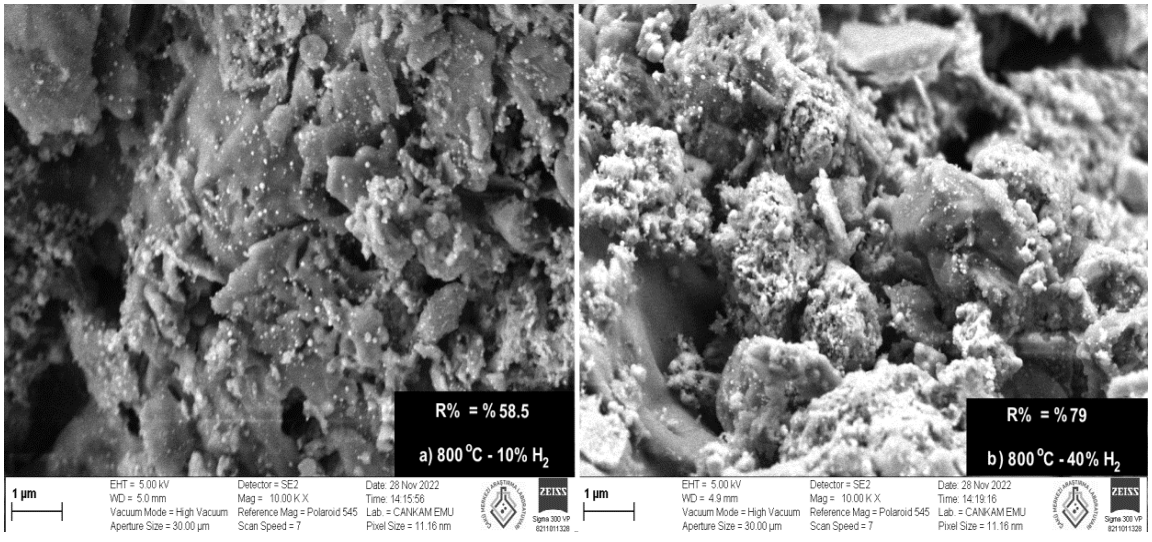

Figure 4.19 SEM images of the samples reduced at 800 ˚C by a) 10% H_2, b) 40% H_2 (Magnification ×10000)

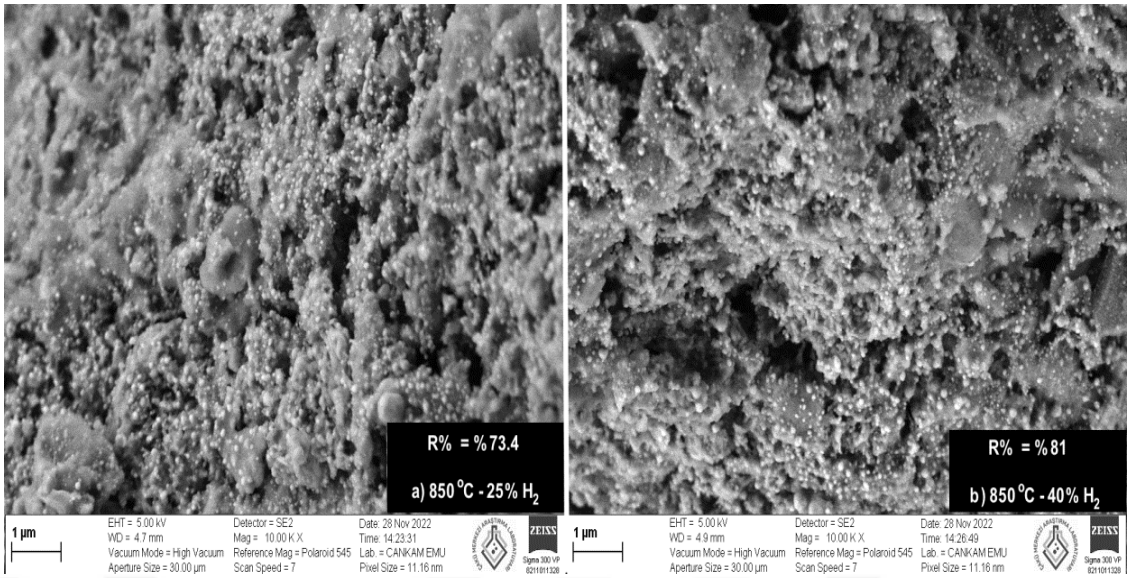

Figure 4.20 SEM images of the samples reduced at 850 ˚C by a) 25% H_2, b) 40% H_2 (Magnification ×10000)

5. CONCLUSIONS AND RECOMMENDATION

The following results were obtained within this study.

1. The highest reduction degree reached during the hydrogen reduction of calcined Gördes laterite ore was 81%.

2. The rate and extend of the reduction reaction was more sensitive to the hydrogen concentration compared to the reaction temperature. The highest conversion levels -almost equal to each other for all temperatures studied-, were obtained in experiments perfomed with 40% hydrogen concentration. This finding strengthened the argument that the reduction process was mostly diffusion-controlled rather than chemical reaction-controlled.

3. The kinetic analysis revealed that the reduction process of calcined Gördes laterite ore with hydrogen was consisted of 3 stages. The first stage proceeded under chemical reaction control, in accordance with the "Contracting Sphere, R3(α)" model, and the second stage proceeded under diffusion control, in accordance with the "One Dimensional Diffusion, D1(α)" model. No mechanism was found to represent the third stage which progressed with an extremely low reaction rate. Furthermore, since the data related to this stage corresponded to the last 3% to 5% of the final conversion levels, it was thought that leaving the third stage out of the kinetic analysis would not bring a major shortcoming in practical terms.

4. The sintered layers which obstracted the gas diffusion and the advanced conversion of the particles which thickened the reduced zone were considered as the causes for the poor reduction behavior of calcined Gördes laterite in the third stage. This claim was verified by the SEM images of the reduced samples which revealed the evolution of the reaction mechanism from chemical reaction-controlled to diffusion-controlled as the reaction advanced.

5. The the activation energy (E_a), the frequency factor (A), and the order of the reaction according to the H_2 concentration was determined as 34.76 kJ/mol, 0.3833 $l^{n-1}.mol^{1-n}.s^{-1}$, and 1.7 for the first stage of the reduction, respectively.

6. The the activation energy (E_a), the frequency factor (A), and the order of the reaction according to the H_2 concentration was determined as 10.18 kJ/mol, 0.0145 $l^{n-1}.mol^{1-n}.s^{-1}$, and 1.4 for the second stage of the reduction, respectively.

REFERENCES

Alsalihi, E. A. T. 2022. Menteş yöresi hematit cevherinin akışkan yatak reaktörde direkt indirgenme kinetiğinin belirlenmesi. MSc. Thesis, Çankırı Karatekin University, 52 pages, Çankırı.

BRITANNICA, 2023. Web site. https://www.britannica.com/science/nickel-chemical-element#/media/1/414238/64439. Date of access: 25.12.2022.

Chen, T. T., Dutrizac, J. E., Krause, E. and Osborne, R. 2004. Mineralogical characterization of nickel laterites from New Caledonia and Indonesia. In International Laterite Nickel Symposium. Wiley, 2(4): 79-99.

Dilmaç N., Yörük, S. and Gülaboğlu, M. Ş. 2012. Determination of reduction degree of direct reduced iron via FT-IR spectroscopy. Vib. Spectrosc., 61: 25-29.

Dilmaç, N. 2021a. Isothermal and non-isothermal reduction kinetics of iron ore oxygen carrier by CO: Modelistic and model-free approaches. Fuel, 296: 120707-120718.

Dilmaç, N. 2021b. Non-isothermal reduction kinetics of Gördes laterite in CO atmosphere. Int. J. Adv. Eng. Pure Sci., 33(4): 677-686.

Elliott, R. and Pickles, C. A. 2017. Thermodynamic analysis of the selective reduction of a nickeliferous limonitic laterite ore by hydrogen. High Temp. Mater. Proc., 36(8): 835-846.

ETSY, 2023. Web site. https://www.etsy.com/listing/1232864389/nickel-element-cube. Date of access: 01.01.2023.

Evans, J.W., Song, S. and Leon-Sucre, C.E. 1976. The kinetics of nickel oxide reduction by hydrogen: Measurements in a fluidized bed and gravimetric apparatus. Metallurgical Transactions B, 7B, March: 55-65.

Farooqui, A. E., Pica, A. M., Marocco, P., Ferrero, D., Lanzini, A., Fiorilli, S., Llorca, J. and Santarelli, M. 2018. Assessment of kinetic model for ceria oxidation for chemical-looping CO_2 dissociation. Chem. Eng. J., 346: 171-181.

Fedunik-Hofman, L., Bayon, A. and Donne, S. W. 2019. Kinetics of solid-gas reactions and their application to carbonate looping systems. Energies, 12 (15): 2981-3016.

IFP ENERGIES NOUVELLES, 2023. Web site. https://www.ifpenergiesnouvelles.com/article/nickel-energy-transition-why-it-called-devils-metal. Date of access: 26.12.2022.

INSIDEXPLORATION, 2023. Web site. https://insidexploration.com/nickel-investment-opportunities-5-junior-mining-companies-to-keep-an-eye-on-as-nickel-gains-traction/. Date of access: 27.12.2022.

Janković, B., Adnadević, B., and Mentus, S. 2007. The kinetic analysis of non-isothermal nickel oxide reduction in hydrogen atmosphere using the invariant kinetic parameters method. Thermochim. Acta, 456(1): 48-55.

Janković, B., Adnadević, B., and Mentus, S. 2008. The kinetic study of temperature-programmed reduction of nickel oxide in hydrogen atmosphere. Chem. Eng. Sci., 63: 567–575.

Li, S. 1999. Study of nickeliferrous laterite reduction. MSc. Thesis, McMaster University, 163 pages, Ontario.

Li, B., Ding, Z., Wei, Y., Wang, H., Yang, Y., and Barati, M. 2018. Kinetics of reduction of low-grade nickel laterite ore using carbon monoxide. Metall. Mater. Trans. B-Process Metall. Mater. Process Sci., 49: 3067–3073.

Liu, D. 2002. Recent development in nickel and cobalt recovery technologies from laterite. Nonferrous Metals (Extractive Metallurgy), 3: 6-10.

Lv, X., Lv, W., Wang, L., and Qiu, J. 2017. Thermal analysis kinetics of the solid-state reduction of nickel laterite ores by carbon. Miner. Met. Mater. Ser., 8: 147-160.

Lv, X., Lv,W., You, Z., Lv, X., and Bai, C. 2018. Non-isothermal kinetics study on carbothermic reduction of nickel laterite ore. Powder Technol., 340: 495-501.

McDonald, R. and Whittington B. 2008. Atmospheric acid leaching of nickel laterites review: Part I. Sulphuric acid technologies. Hydrometallurgy, 91(1): 35-55.

MTA, 2018. Web site. https://www.mta.gov.tr/v3.0/sayfalar/bilgi- merkezi/maden-serisi/img/Nikel.pdf. Date of access: 10.05.2022.

MTA, 2023. Web site. https://www.mta.gov.tr/v3.0/sayfalar/hizmetler/images/b_h/nikl_man_anti.jpg. Date of access: 13.10.2022.

NICKEL INSTITUTE, 2023. Web site. https://nickelinstitute.org/en/about-nickel-and-its-applications/#01-nickel-properties. Date of access: 18.11.2022.

Norgate, T. and Jahanshahi, S. 2011. Assessing the energy and greenhouse gas footprints of nickel laterite processing. Minerals Engineering, 24(7): 698-707.

SLIDESERVE, 2023. Web site. https://www.slideserve.com/kaili/nickel-laterites-

characteristics-classification-and-processing-options. Date of access: 01.01.2023.

Su, M., Ma, J., Tian, X. and Zhao, H. 2017. Reduction kinetics of hematite as oxygen carrier in chemical looping combustion. Fuel Process. Technol., 155: 160-167.

Szekely, J. and Evans, J.W. 1970. A structural model for gas-solid reactions with a moving boundary. Chem. Eng. Sci., 25: 1091-1107.

USGS, 2011. Web site. https://pubs.usgs.gov/of/2011/1058/. Date of access: 01.01.2023.

Valix, M., Tang, J. Y. and Cheung, W. H. 2001. The effects of mineralogy on the biological leaching of nickel laterite ores. Minerals Engineering, 14(12): 1629-1635.

Wang, X., Sun, T., Chen, C., and Hu, T. 2017. Current studies of treating processes for nickel laterite ores, Advances in Computer Science Research, 70: 139-152.

Whittington, B. I. and Muir, D. 2000. Pressure acid leaching of nickel laterites: a review. Mineral Processing and Extractive Metullargy Review, 21(6): 527-599.

WOODMAC, 2023. Web site. https://www.woodmac.com/news/opinion/nickel-and-copper-building-blocks-for-a-greener-future/. Date of access: 01.01.2023.

Yang, S., Du, W., Shi, P., Shangguan, J., Liu, S., and Zhou, C. 2016. Mechanistic and kinetic analysis of Na2SO4 -Modified laterite decomposition by thermogravimetry coupled with mass spectrometry. PLoS One, 11(6): 1-21.

Zhai, X., Fu, Y., Zhang, X., Ma, L. and Xie, F. 2009. Intensification of sulphation and pressure acid leaching of nickel laterite by microwave radiation. Hydrometallurgy, 99(3-4): 189-193.

Zhang, Y., Cui, K., Wang, J., Wang, X., Qie, J., and Xu, Q. 2020. Effects of direct reduction process on the microstructure and reduction characteristics of carbon-bearing nickel laterite ore pellets. Powder Technol., 376: 496-506.

Zhou, Q. 2005. Current Situation and Development Direction of Technology for Oxidized Nickel Ore Treatment. Yunnan Metallurgy, 34(6): 33-36.

Zhu, D., Pan, L., Guo, Z., Pan, J., and Zhang, F. 2019. Utilization of limonitic nickel laterite to produce ferronickel concentrate by the selective reduction-magnetic separation process. Adv. Powder Technol., 30: 451–460.